

Innovation in Underwater Robots

Biologically Inspired Swimming Snake Robots



IMAGE LICENSED BY INGRAM PUBLISHING

By Eleni Kerasidi, Pål Liljebäck, Kristin Y. Pettersen,
and Jan Tommy Gravdahl

Increasing efficiency by improving locomotion methods is a key issue for underwater robots. Moreover, a number of different control design challenges must be solved to realize operational swimming robots for underwater tasks. This article proposes and experimentally validates a straight-line-path-following controller for biologically inspired swimming snake robots. In particular, a line-of-sight (LOS) guidance law is presented, which is combined with a

sinusoidal gait pattern and a directional controller that steers the robot toward and along the desired path. The performance of the path-following controller is investigated through experiments with a physical underwater snake robot for both lateral undulation and eel-like motion. In addition, fluid parameter identification is performed, and simulation results based on the identified fluid coefficients are presented to obtain a back-to-back comparison with the motion of the physical robot during the experiments. The experimental results show that the proposed control strategy successfully steers the robot toward and along the desired path for both lateral undulation and eel-like motion patterns.

Digital Object Identifier 10.1109/MRA.2015.2506121
Date of publication: 8 March 2016

Biologically Inspired Swimming Snake Robots

The use of robotic underwater vehicles has rapidly increased during the last several decades due to technological innovations that enable these mechanisms to operate in deep and harsh subsea environments. Today autonomous underwater vehicles (AUVs) and remotely operated vehicles (ROVs) are widely used subsea for different challenging tasks [1], such as inspection, surveillance, maintenance, repair, and construction, and they are extensively used in the subsea oil and gas industry and by the science community. Swimming snake robots represent an interesting alternative to conventional ROVs and AUVs.

For centuries, engineers and scientists have gained inspiration from the natural world in their search for solutions to technical problems, a process termed *biomimetics*. To this end, inspired by biological swimming creatures, underwater snake robots carry the potential of meeting the growing need for robotic mobility in underwater environments. These mechanisms have a long, slender, and flexible body, enabling them to reach and operate in locations not accessible by larger and more conventional underwater vehicles. At the same time, a swimming snake robot carries manipulation capabilities as an inherent part of its body since it is essentially a mobile manipulator arm. Underwater snake robots thus have the potential to improve the efficiency and maneuverability of modern-day underwater vehicles. A particularly relevant application concerns inspection and maintenance of subsea oil and gas installations, where the ability to reach tight locations in between pipe structures is important. Moreover, for the biological community and marine archeology, snake robots that can swim smoothly with limited noise and navigate in difficult environments such as shipwrecks are very interesting [2]. To realize operational snake robots for such underwater applications, a number of different control design challenges must first be solved. An important control problem concerns the ability to follow given reference paths, and this is the topic of this article.

Work on biologically inspired snake robots was at first largely restricted to land-based studies, for which reviews on modeling, implementation, and control of snake robots have been presented in [3]–[5]. Empirical and analytic studies of snake locomotion were reported by [6], while the work of [7] is among the first approaches to develop a snake robot prototype. Several land-based snake robots [8]–[10] and biologically inspired swimming robots [11]–[19] have been constructed since then. Due to the complex dynamics of swimming snake robots, several different modeling approaches have been carried out in the literature [2], [14], [20]–[28]. Several results have been reported in the related field of design, modeling, and control of underwater robots that mimic the movement of fish [18], [19], [29]–[32]. In addition, sandfish lizard locomotion has been studied as the inspiration for a robot design in [33]. A comparison of these approaches is presented in [34].

Most modeling approaches for underwater snake robots omit the fluid moments (fluid torques) by considering that

their effect on the motion of the robot is negligible [22], [26], [35]. However, including the impact of the fluid torques on the power consumption of the system (see, e.g., [25]), will improve the accuracy of the model from a hydrodynamic and energy-efficiency point of view. The works in [23], [25], and [36] propose the modeling of fluid torques, with the drag force and torque evaluated numerically. These approaches lack a closed-form solution, which is a drawback since a hydrodynamic model in closed form is advantageous for model-based analysis and control design. The works in [2], and [37] present a closed-form hydrodynamic model, where hydrodynamic forces and torques are considered and where there is no need for algorithmic computations of drag effects. Furthermore, in this approach, both linear and nonlinear drag forces (resistive fluid forces), the added mass effect (reactive fluid forces), the fluid moments, and current effects are considered. The resulting closed-form model is well suited for model-based control design schemes. In this article, the adopted control design will be based on the model presented in [2] and [37].

Previous control approaches for underwater snake robots proposed in the literature have mainly been concerned with forward and turning locomotion [14], [38]. Thus, the next step would be path-following control. To this end, [22], [39], and [18] propose controllers for tracking straight and curved trajectories based on synthesizing gaits for translational and rotational motion of various fish-like mechanisms. The evolution from fish to amphibian using the same concept is presented in [13] by employing central pattern generators. Moreover, [22] and [40] propose controllers for tracking straight and curved trajectories for eel-like motion. In [41], the path to be followed by the underwater snake robot is defined by straight lines of interconnected points, combining an artificial potential field-based path planner with a new waypoint guidance strategy. A different waypoint guidance strategy is described in [42] for a carangiform swimmer, having the waypoints defined a priori.

Several previous works consider control schemes for eel-like robot locomotion. In particular, [43] develops a feedback control scheme for three-dimensional (3-D) movement of the robot's continuous model presented in [23]. In [44], motion control of a 3-D eel-like robot without pectoral fins is described, while in [45] a multivariable constrained feedback control scheme is proposed, considering a reduced model of an eel robot. A methodology for path following of eel-like robots is presented in [46] based on autonomous gait generation extracted from the controlled local system curvature. Open-loop motion planning for eel-like robots is presented in [14], [22], and [38], including the experimental evaluation of the adopted techniques. Furthermore, in [22], experiments for closed-loop straight-line tracking using image-based position feedback are implemented with disturbance rejection in the plane. Nevertheless, these preliminary experiments were not satisfactory, as mentioned in [22], although they prove the general concept. In [34], an underwater snake robot is commanded to track a straight-line path in the presence of ocean currents of unknown direction and magnitude, controlled by

an integral LOS path-following controller. The presented experimental results confirmed that the proposed integral LOS guidance law can be applied to underwater snake robots not only to achieve tracking of straight lines but also to compensate for ocean drift effects, including current effects.

Another important control problem for underwater vehicles concerns the ability to achieve efficient motion with preferably a minimum amount of consumed energy to be able to undertake longer missions. Hence, for the long-term autonomy of underwater vehicles, energy efficiency is one of the main challenges. Solutions in this direction are proposed in [47] and [48]. In particular, in [47], the relationships between the parameters of the gait patterns, the consumed energy, and the forward velocity for different motion patterns for underwater snake robots were investigated. In addition, empirical rules were proposed to choose the most efficient motion pattern. In [48], a simulation study was undertaken to compare the power consumption of swimming snake robots with that of today's benchmark solution for subsea inspection, maintenance, and repair, which are ROVs. The presented simulation results showed that, with respect to the cost of transportation metric and the total consumed energy, the underwater snake robots are more energy efficient than an ROV for all the compared motion modes.

This article considers path-following control of swimming snake robots. Based on the dynamic model presented

in [2] and [37], we formulate an LOS path-following controller for steering an underwater snake robot along a straight-line path. The LOS guidance law is inspired by path-following control of marine surface vessels [1], which is widely used for directional control of these vessels. A preliminary investigation of the control strategy was presented in [41], but whereas the efficacy of the control strategy is supported by simulation results in [41], this article investigates its efficacy through experiments with a physical underwater snake robot [17].

The first contribution of this article are the experimental results, which show that the LOS guidance law can be applied to underwater snake robots to achieve straight-line path following for both lateral undulation and eel-like motion patterns. This contribution extends our previous work in [34], where a less extensive experimental study was carried out for the case of lateral undulation motion only. Lateral undulation and eel-like motion are both highly relevant motion patterns for underwater snake robots. An experimental study considering both motion patterns is therefore interesting since it allows the two motion patterns to be compared.

The second contribution of this article is a comparative study between the experimental results and the corresponding simulation results. In particular, the experimental results are compared with simulation results that are obtained after carrying out fluid parameter identification of the model presented in [2] and [37]. Whereas the simulation study in [41] was carried out by considering theoretical values for the fluid parameters, this article presents preliminary experimental results obtained for the fluid coefficients using a physical underwater snake robot [17], thereby allowing us to obtain an accurate back-to-back comparison of real experimental and simulated data. This gives us the opportunity to obtain not only qualitative comparison results as in [34] and [41] but also a quantitative comparison between the motion of the simulated and the physical snake robot.

In [14], simulation results of a fish-like robot with the caudal tail named AmphiBot III were obtained via numerical integration in real time and compared with experimental results by calibrating the fluid coefficients. By using the large amplitude elongated body theory, [14] also considers the reaction force exerted on the caudal fin in conjunction with swimming locomotion. In this article, however, we assume a cylindrical shape for all links including the tail, so that an explicit tail model is not considered. Furthermore, we present preliminary results for the fluid coefficients identification for the model presented in [2] and [37]. To the best of our knowledge, experimental validation of a complex fluid model that takes into account both the reactive (added mass effects) and resistive forces (combination of linear and nonlinear drag forces) and is expressed in closed form has not yet been investigated in the literature. Moreover, in this article we propose a solution for path following of underwater snake robots supported by simulation and experimental results. Experimental results show that the snake robot is able to follow the reference path both for lateral undulation and eel-like

Table 1. The definitions of mathematical terms.

Symbol	Description	Vector
n	The number of links	
l	The half length of a link	
m	Mass of each link	
J	Moment of inertia of each link	
θ_i	Angle between link i and the global x-axis	$\theta \in \mathbb{R}^n$
ϕ_i	Angle of joint i	$\phi \in \mathbb{R}^{n-1}$
(x_i, y_i)	Global coordinates of the CM of link i	$\mathbf{X}, \mathbf{Y} \in \mathbb{R}^n$
(p_x, p_y)	Global coordinates of the CM of the robot	$\mathbf{P}_{\text{CM}} \in \mathbb{R}^2$
u_i	Actuator torque of joint between link i and link $i+1$	$\mathbf{u} \in \mathbb{R}^{n-1}$
u_{i-1}	Actuator torque of joint between link i and link $i-1$	$\mathbf{u} \in \mathbb{R}^{n-1}$
$f_{x,i}$	Fluid force on link i in x-direction	$\mathbf{f}_x \in \mathbb{R}^n$
$f_{y,i}$	Fluid force on link i in y-direction	$\mathbf{f}_y \in \mathbb{R}^n$
τ_i	Fluid torque on link i	$\tau \in \mathbb{R}^n$
$h_{x,i}$	Joint constraint force in x-direction on link i from link $i+1$	$\mathbf{h}_x \in \mathbb{R}^{n-1}$
$h_{y,i}$	Joint constraint force in y-direction on link i from link $i+1$	$\mathbf{h}_y \in \mathbb{R}^{n-1}$
$h_{x,i-1}$	Joint constraint force in x-direction on link i from link $i-1$	$\mathbf{h}_x \in \mathbb{R}^{n-1}$
$h_{y,i-1}$	Joint constraint force in y-direction on link i from link $i-1$	$\mathbf{h}_y \in \mathbb{R}^{n-1}$

motion, and using the results presented in [47] and [48] regarding the power efficiency of the underwater snake robots, we can argue that underwater swimming robots can be considered good candidates for different challenging tasks in the sub-sea environment.

Mathematical Model of Underwater Snake Robot

This section briefly presents a model of the kinematics and dynamics of an underwater snake robot moving in a virtual horizontal plane, which will be used in the control design and analysis of this article. A more detailed presentation of the model can be found in [2] and [37].

Notations and Defined Symbols

The underwater snake robot consists of n rigid links of equal length $2l$ interconnected by $n - 1$ joints. The links are assumed to have the same mass m and moment of inertia $J = 1/3ml^2$. The mass of each link is uniformly distributed so that the link center of mass (CM) is located at its center point (at length l from the joint at each side). The total mass of the snake robot is, therefore, nm . In the following sections, the kinematics and dynamics of the robot will be described in terms of the mathematical symbols listed in Table 1 and illustrated in Figures 1 and 2. The following vectors and matrices are used in the subsequent sections:

$$\mathbf{A} = \begin{bmatrix} 1 & 1 & & \\ & \ddots & \ddots & \\ & & 1 & 1 \end{bmatrix}, \quad \mathbf{D} = \begin{bmatrix} 1 & -1 & & \\ & \ddots & \ddots & \\ & & 1 & -1 \end{bmatrix},$$

where $\mathbf{A}, \mathbf{D} \in \mathbb{R}^{(n-1) \times n}$. Furthermore,

$$\begin{aligned} \mathbf{e} &= [1 \dots 1]^T \in \mathbb{R}^n, \\ \mathbf{E} &= \begin{bmatrix} \mathbf{e} & \mathbf{0}_{n \times 1} \\ \mathbf{0}_{n \times 1} & \mathbf{e} \end{bmatrix} \in \mathbb{R}^{2n \times 2}, \\ \mathbf{S}_\theta &= \text{diag}(\sin \theta) \in \mathbb{R}^{n \times n}, \\ \mathbf{C}_\theta &= \text{diag}(\cos \theta) \in \mathbb{R}^{n \times n}, \\ \dot{\theta}^2 &= [\dot{\theta}_1^2 \dots \dot{\theta}_n^2]^T \in \mathbb{R}^n, \\ \mathbf{K} &= \mathbf{A}^T (\mathbf{DD}^T)^{-1} \mathbf{D}. \end{aligned}$$

The matrices \mathbf{A} and \mathbf{D} represent, respectively, an addition and a difference matrix, which will be used for adding and subtracting pairs of adjacent elements of a vector. Furthermore, the vector \mathbf{e} represents a summation vector, which is used for adding all elements of an n -dimensional vector.

Kinematics of Underwater Snake Robot

The snake robot is assumed to move in a virtual horizontal plane, fully immersed in water, and has $n + 2$ degrees of freedom (n

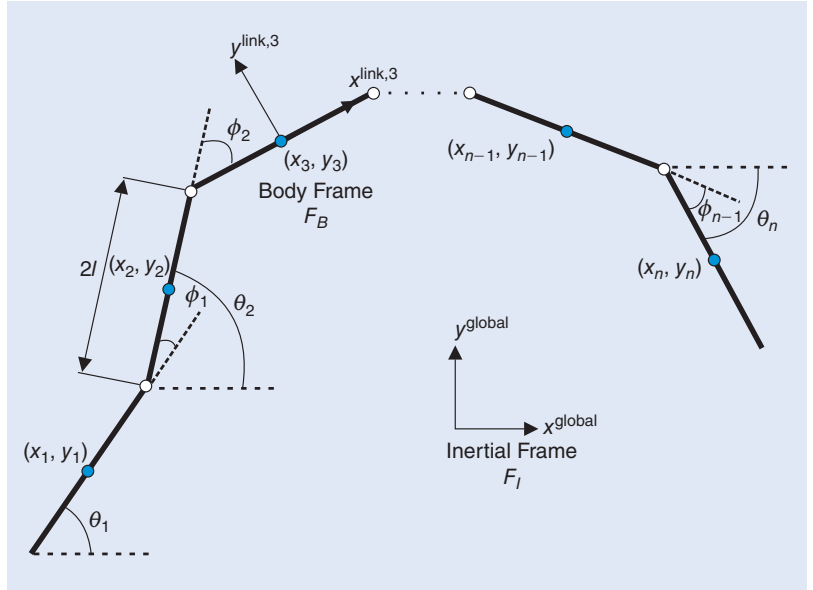


Figure 1. The kinematic parameters of the underwater snake robot.

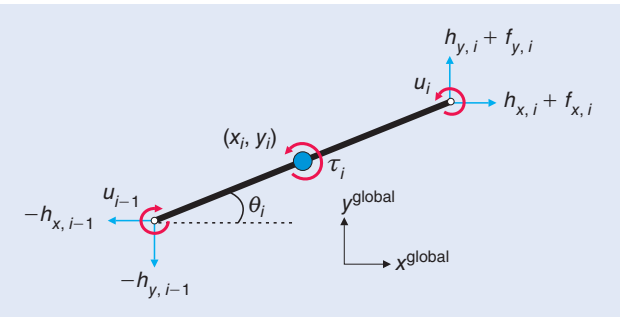


Figure 2. The forces and torques acting on each link of the underwater snake robot.

links angles and the $x - y$ position of the robot). The link angle of each link $i \in 1, \dots, n$ of the snake robot is denoted by $\theta_i \in \mathbb{R}$, while the joint angle of joint $i \in 1, \dots, n - 1$ is given by

$$\phi_i = \theta_i - \theta_{i-1}. \quad (1)$$

The link angles and the joint angles are assembled in the vectors $\boldsymbol{\theta} = [\theta_1, \dots, \theta_n]^T \in \mathbb{R}^n$ and $\boldsymbol{\phi} = [\phi_1, \dots, \phi_{n-1}]^T \in \mathbb{R}^{n-1}$, respectively. The heading (or orientation) $\bar{\theta} \in \mathbb{R}$ of the snake is defined as the average of the link angles, i.e., as [3]

$$\bar{\theta} = \frac{1}{n} \sum_{i=1}^n \theta_i. \quad (2)$$

The global frame position $\mathbf{p}_{\text{CM}} \in \mathbb{R}^2$ of the CM of the robot is given by

$$\mathbf{p}_{\text{CM}} = \begin{bmatrix} p_x \\ p_y \end{bmatrix} = \begin{bmatrix} \frac{1}{nm} \sum_{i=1}^n mx_i \\ \frac{1}{nm} \sum_{i=1}^n my_i \end{bmatrix} = \frac{1}{n} [\mathbf{e}^T \mathbf{X}], \quad (3)$$

where (x_i, y_i) are the global frame coordinates of the CM of link i , $\mathbf{X} = [x_1, \dots, x_n]^T \in \mathbb{R}^n$ and $\mathbf{Y} = [y_1, \dots, y_n]^T \in \mathbb{R}^n$.

The forward velocity of the robot is denoted by $\bar{v}_t \in \mathbb{R}$ and is defined as the component of the CM velocity along the current heading of the snake, i.e.,

$$\bar{v}_t = \dot{p}_x \cos \theta + \dot{p}_y \sin \theta. \quad (4)$$

Hydrodynamic Modeling

As has been noted in the biorobotics community, underwater snake (eel-like) robots bring a promising prospective to improve the efficiency and maneuverability of modern-day underwater vehicles. The dynamic modeling of the contact forces however, is quite complicated compared to the modeling of the overall rigid motion. The Navier–Stokes equations are very difficult to solve and not suited for robotics control design purposes. The hydrodynamic modeling approach from [2] that is considered in this article takes into account both the linear and the nonlinear drag forces (resistive fluid forces), the added mass effect (reactive fluid forces), the fluid moments, and current effects.

In [2], it is shown that the fluid forces on all links can be expressed in vector form as

$$\mathbf{f} = \begin{bmatrix} \mathbf{f}_x \\ \mathbf{f}_y \end{bmatrix} = \begin{bmatrix} \mathbf{f}_{A_x} \\ \mathbf{f}_{A_y} \end{bmatrix} + \begin{bmatrix} \mathbf{f}_{D_x}^I \\ \mathbf{f}_{D_y}^I \end{bmatrix} + \begin{bmatrix} \mathbf{f}_{D_x}^{II} \\ \mathbf{f}_{D_y}^{II} \end{bmatrix}. \quad (5)$$

The vectors \mathbf{f}_{A_x} and \mathbf{f}_{A_y} represent the effects from added mass forces and are expressed as

$$\begin{bmatrix} \mathbf{f}_{A_x} \\ \mathbf{f}_{A_y} \end{bmatrix} = - \begin{bmatrix} \mu_n (\mathbf{S}_\theta)^2 & -\mu_n \mathbf{S}_\theta \mathbf{C}_\theta \\ -\mu_n \mathbf{S}_\theta \mathbf{C}_\theta & \mu_n (\mathbf{C}_\theta)^2 \end{bmatrix} \begin{bmatrix} \ddot{\mathbf{X}} \\ \ddot{\mathbf{Y}} \end{bmatrix} - \begin{bmatrix} -\mu_n \mathbf{S}_\theta \mathbf{C}_\theta & -\mu_n (\mathbf{S}_\theta)^2 \\ \mu_n (\mathbf{C}_\theta)^2 & \mu_n \mathbf{S}_\theta \mathbf{C}_\theta \end{bmatrix} \begin{bmatrix} \mathbf{V}_x^a \\ \mathbf{V}_y^a \end{bmatrix} \dot{\theta}, \quad (6)$$

where $\mathbf{V}_x^a = \text{diag}(V_{x,1}, \dots, V_{x,n}) \in \mathbb{R}^{n \times n}$, $\mathbf{V}_y^a = \text{diag}(V_{y,1}, \dots, V_{y,n}) \in \mathbb{R}^{n \times n}$ and $[V_{x,i}, V_{y,i}]^T$ is the current velocity expressed in inertial frame coordinates. The drag forces on the robot are given by

$$\begin{bmatrix} \mathbf{f}_{D_x}^I \\ \mathbf{f}_{D_y}^I \end{bmatrix} = - \begin{bmatrix} c_t \mathbf{C}_\theta & -c_n \mathbf{S}_\theta \\ c_t \mathbf{S}_\theta & c_n \mathbf{C}_\theta \end{bmatrix} \begin{bmatrix} \mathbf{V}_{r_x} \\ \mathbf{V}_{r_y} \end{bmatrix} \quad (7)$$

$$\begin{bmatrix} \mathbf{f}_{D_x}^{II} \\ \mathbf{f}_{D_y}^{II} \end{bmatrix} = - \begin{bmatrix} c_t \mathbf{C}_\theta & -c_n \mathbf{S}_\theta \\ c_t \mathbf{S}_\theta & c_n \mathbf{C}_\theta \end{bmatrix} \text{sgn}\left(\begin{bmatrix} \mathbf{V}_{r_x} \\ \mathbf{V}_{r_y} \end{bmatrix}\right) \begin{bmatrix} \mathbf{V}_{r_x}^2 \\ \mathbf{V}_{r_y}^2 \end{bmatrix}, \quad (8)$$

where $\mathbf{f}_{D_x}^I$, $\mathbf{f}_{D_y}^I$, $\mathbf{f}_{D_x}^{II}$, $\mathbf{f}_{D_y}^{II}$ are the linear and nonlinear drag forces, respectively, and where the relative link velocities \mathbf{V}_{r_x} and \mathbf{V}_{r_y} are given by

$$\begin{bmatrix} \mathbf{V}_{r_x} \\ \mathbf{V}_{r_y} \end{bmatrix} = \begin{bmatrix} \mathbf{C}_\theta & \mathbf{S}_\theta \\ -\mathbf{S}_\theta & \mathbf{C}_\theta \end{bmatrix} \begin{bmatrix} \dot{\mathbf{X}} - \mathbf{V}_x \\ \dot{\mathbf{Y}} - \mathbf{V}_y \end{bmatrix}. \quad (9)$$

In addition, the fluid torques on all links are

$$\tau = -\Lambda_1 \ddot{\theta} - \Lambda_2 \dot{\theta} - \Lambda_3 \dot{\theta} |\dot{\theta}|, \quad (10)$$

where $\Lambda_1 = \lambda_1 \mathbf{I}_n$, $\Lambda_2 = \lambda_2 \mathbf{I}_n$ and $\Lambda_3 = \lambda_3 \mathbf{I}_n$. The coefficients c_t , c_n , λ_2 , λ_3 represent the drag forces parameters due to the pressure difference between the two sides of the body, and the parameters μ_n , λ_1 represent the added mass of the

fluid carried by the moving body. Note that the added mass parameter in the x -direction is considered equal to zero ($\mu_t = 0$) because the added mass of a slender body in the longitudinal direction can be neglected compared to the body mass [2].

Equations of Motion

This section presents the equations of motion for the underwater snake robot. In [2] and [37], it is shown that the acceleration of the CM may be expressed as

$$\begin{bmatrix} \ddot{p}_x \\ \ddot{p}_y \end{bmatrix} = -\mathbf{M}_p \begin{bmatrix} \mathbf{k}_{11} & \mathbf{k}_{12} \\ \mathbf{k}_{21} & \mathbf{k}_{22} \end{bmatrix} \begin{bmatrix} I\mathbf{K}^T(\mathbf{C}_\theta \dot{\theta}^2 + \mathbf{S}_\theta \ddot{\theta}) \\ I\mathbf{K}^T(\mathbf{S}_\theta \dot{\theta}^2 - \mathbf{C}_\theta \ddot{\theta}) \end{bmatrix} - \mathbf{M}_p \begin{bmatrix} \mathbf{k}_{12} & -\mathbf{k}_{11} \\ \mathbf{k}_{22} & -\mathbf{k}_{21} \end{bmatrix} \begin{bmatrix} \mathbf{V}_x^a \\ \mathbf{V}_y^a \end{bmatrix} \dot{\theta} + \mathbf{M}_p \begin{bmatrix} \mathbf{e}^T \mathbf{f}_{Dx} \\ \mathbf{e}^T \mathbf{f}_{Dy} \end{bmatrix}, \quad (11)$$

where the detailed derivation of the matrix \mathbf{M}_p and vectors \mathbf{k}_{11} , \mathbf{k}_{12} , \mathbf{k}_{21} , and \mathbf{k}_{22} are given in [2] and [37]. In addition, it is shown that, under the influence of fluid forces (5) and torques (10), the complete equations of motion of the underwater snake robot are obtained by (11) and

$$\begin{aligned} \mathbf{M}_\theta \ddot{\theta} + \mathbf{W}_\theta \dot{\theta}^2 + \mathbf{V}_\theta \dot{\theta} + \Lambda_3 |\dot{\theta}| \dot{\theta} \\ + \mathbf{K}_{Dx} \mathbf{f}_{Dx} + \mathbf{K}_{Dy} \mathbf{f}_{Dy} = \mathbf{D}^T \mathbf{u}, \end{aligned} \quad (12)$$

with $\mathbf{f}_{Dx} = \mathbf{f}_{Dx}^I + \mathbf{f}_{Dx}^{II}$ and $\mathbf{f}_{Dy} = \mathbf{f}_{Dy}^I + \mathbf{f}_{Dy}^{II}$ representing the drag forces in x - and y -directions, and $\mathbf{u} \in \mathbb{R}^{n-1}$ the control input. For more details and the derivation of the matrices \mathbf{M}_θ , \mathbf{W}_θ , \mathbf{V}_θ , \mathbf{K}_{Dx} and \mathbf{K}_{Dy} , see [37].

By introducing the state variable $\mathbf{x} = [\theta^T, \mathbf{p}_{CM}^T, \dot{\theta}^T, \dot{\mathbf{p}}_{CM}^T]^T \in \mathbb{R}^{2n+4}$, we can rewrite the model of the robot compactly in state-space form as

$$\dot{\mathbf{x}} = [\dot{\theta}^T, \dot{\mathbf{p}}_{CM}^T, \ddot{\theta}^T, \ddot{\mathbf{p}}_{CM}^T]^T = \mathbf{F}(\mathbf{x}, \mathbf{u}), \quad (13)$$

where the elements of $\mathbf{F}(\mathbf{x}, \mathbf{u})$ are found by solving (11) and (12) for $\ddot{\mathbf{p}}_{CM}$ and $\ddot{\theta}$, respectively.

Remark 1

It is interesting to note that if, in the dynamic model (11) and (12), we set the fluid parameters to zero and replace the drag forces in the x - and y -direction with ground friction models [3], then the model exactly reduces to the dynamic model of a ground snake robot described in [3]. The underwater snake robot model is thus an extension of the land snake robot model and may be used for amphibious snakes moving both on land and in water.

LOS Path-Following Control

In this section, we present an LOS path-following control scheme for underwater snake robots moving in a virtual horizontal plane [41], based on the general sinusoidal motion pattern proposed in [49]. In particular, a function to describe a quite general class of sinusoidal motion patterns suitable for locomotion of underwater snake robots was derived in [49] and is briefly presented in the “Outer-Loop Controller” section.

The structure of the LOS path-following controller, as shown in Figure 3, consists of two parts, the inner-loop proportional-derivative (PD) controller that is used to control the joint angles ϕ and the outer-loop controller that is used for generating the reference joint angles to achieve the desired sinusoidal gait pattern and the desired heading $\bar{\theta}_{ref}$. The latter controller is composed of three separate components: 1) the gait-pattern generator, which extracts the sinusoidal motion pattern to propel the robot forward; 2) the heading controller, which steers the robot toward and, subsequently, along the desired path; and 3) the LOS guidance law (Figure 4), which generates the desired heading angle to reach and follow the desired path. These three components of the path-following controller will be presented in the following sections.

Control Objective

The main control objective is the convergence of the robot to the desired straight-line path. The forward velocity \bar{v}_t of the robot, defined in (4), does not require accurate control but only $\bar{v}_t > 0$ to ensure a nonzero forward velocity for the robot. Regarding the position of the robot in the two-dimensional (2-D) plane, the desired path is aligned with the global x -axis for simplicity, and thus the cross-track error along the desired path coincides with the robot's position over the global y -axis. Note that the controller can easily be generalized to follow a straight line in any direction by redefining the global x -axis with a proper rotational transformation. Furthermore, the heading of the robot (2) corresponds to the angle formed between the robot's body and the desired straight-line path (Figure 4). Considering these objectives, the control system can be formalized as

$$\lim_{t \rightarrow \infty} p_y = 0 \quad (14)$$

$$\lim_{t \rightarrow \infty} \bar{\theta} = 0 \quad (15)$$

$$\lim_{t \rightarrow \infty} \bar{v}_t > 0. \quad (16)$$

Note that, since underwater snake robots have an oscillatory gait pattern, the control objectives imply that p_y and $\bar{\theta}$ should have steady-state oscillations of about zero.

Remark 2

As we have already mentioned, in this article, forward speed control has not been considered. However, in [47], based on extensive simulation results, we showed how it is possible to achieve a desired forward velocity for underwater snake robots by simply choosing a proper set for the gait parameters α, ω and δ . In the future, a formal control approach for speed control should be investigated.

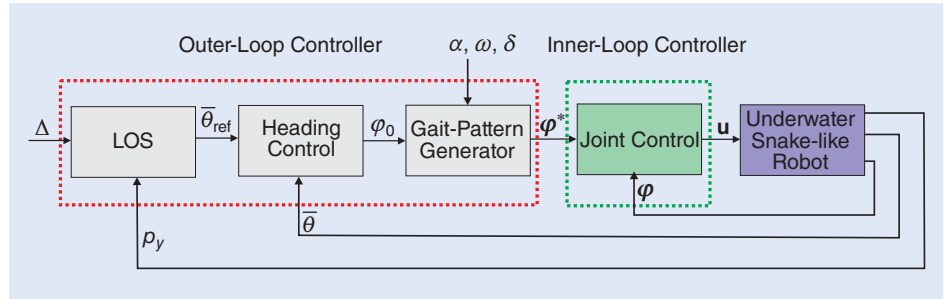


Figure 3. The structure of the LOS path-following controller.

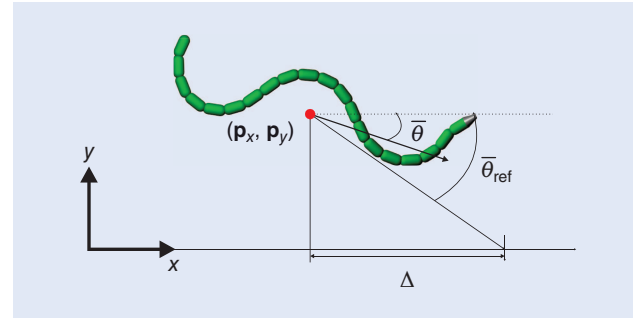


Figure 4. An illustration of the LOS guidance law.

Motion Pattern

Previous studies on swimming snake robots have focused on two motion patterns: lateral undulation and eel-like motion. In the present study, the adopted motion pattern is a more general sinusoidal motion pattern, which represents a broader class, including the aforementioned ones. Lateral undulation [3] constitutes the fastest and most common type of ground snake locomotion. It is achieved by means of body waves with a constant amplitude, propagated from head to tail, while the snake robot is commanded to follow the serpentine curve [7]. On the other hand, an eel-like motion can be achieved by propagating lateral axial undulations with increasing amplitude from head to tail [29]. To achieve the general sinusoidal motion pattern, each joint $i \in \{1, \dots, n - 1\}$ of the underwater snake robot is commanded to track the reference signal

$$\phi_i^*(t) = \alpha g(i, n) \sin(\omega t + (i - 1)\delta) + \phi_0, \quad (17)$$

where α and ω are the maximum amplitude and the frequency, respectively; δ determines the phase shift between the joints; and the function $g(i, n)$ is a scaling function for the amplitude of joint i [49]. This scaling function allows (17) to describe a quite general class of sinusoidal functions, including several different snake motion patterns. For instance, $g(i, n) = 1$ gives lateral undulation, while $g(i, n) = (n - i)/(n + 1)$ gives eel-like motion [2]. Finally, the parameter ϕ_0 is a joint offset coordinate that is shown to affect the direction of locomotion in the case of land-based snake robots [3] and fish robots [42] as well. In this article, the joint offset will be used to control the direction of the locomotion of underwater snake robots.

Outer-Loop Controller

As noted previously, the outer-loop controller generates the reference joint angles to achieve the desired sinusoidal gait pattern and the desired orientation for the robot. Regarding the sinusoidal gait pattern, previous approaches keep the parameters α and δ fixed, while ω and ϕ_0 are used to control the speed and the direction of the snake robot, respectively, [3], [42], [50]. In this article, the same approach will be adopted. The orientation $\bar{\theta}$ of the robot is given by (2). Moreover, for the desired orientation, motivated by [51] and [1], we propose to define the reference orientation using the following LOS guidance law

$$\bar{\theta}_{\text{ref}} = -\arctan\left(\frac{p_y}{\Delta}\right), \quad \Delta > 0, \quad (18)$$

where p_y is the cross-track error (i.e., the position of the underwater snake robot along the global y -axis), while Δ is a constant design parameter. In particular, Δ denotes the look-ahead distance that influences the rate of convergence to the desired path [1]. Note that LOS guidance laws are much used in practice for path-following control of marine surface vessels [1], [52] and have been used for path-following control of ground snake robots [3].

Remark 3

The look-ahead distance Δ is a fundamental parameter for the LOS guidance law since this parameter directly affects the transient motion of the underwater snake robot. A large value of Δ results in a well-damped transient motion, but the convergence to the desired path becomes slow (Figure 4). In contrast, a too small value of Δ forces the system to have a poor or unstable performance. A rule of thumb is to define a value for Δ larger than twice the length of the robot (see [1]).

Motivated by the effective application of LOS guidance laws for path-following control of marine surface vessels [1], [52] and especially in the corresponding case of ground snake robots [3], we choose the joint angle offset ϕ_0 as

$$\phi_0 = k_\theta (\bar{\theta} - \bar{\theta}_{\text{ref}}), \quad (19)$$

where $k_\theta > 0$ is a control gain [37].

Inner-Loop Controller

To make the joint angle ϕ_i follow its reference signal ϕ_i^* , a PD controller is used:

$$u_i = \ddot{\phi}_i^* + k_d(\dot{\phi}_i^* - \dot{\phi}_i) + k_p(\phi_i^* - \phi_i), \quad i = 1, \dots, n-1, \quad (20)$$

where $k_p > 0$ and $k_d > 0$ are the gains of the controller.

Note that, for the experimental and the simulation results presented in the following sections, the values of the gait parameters α , ω , and δ in (17) and the controller gains, k_p and k_d in (20) are chosen arbitrarily based on our experience on undulatory motion of underwater snake robots. In the future, optimization techniques may be used for choosing the optimal gait parameters, and, preferably, the controller gains should be based on the model-based analysis.

Experimental Setup

This section describes the experimental setup employed for the fluid parameter identification and the investigation of the performance of the LOS path-following controller proposed in [41].

Underwater Snake Robot—Mamba

In this section, the underwater snake robot that was used in our experiments is presented. A more detailed description of the robot can be found in [17].

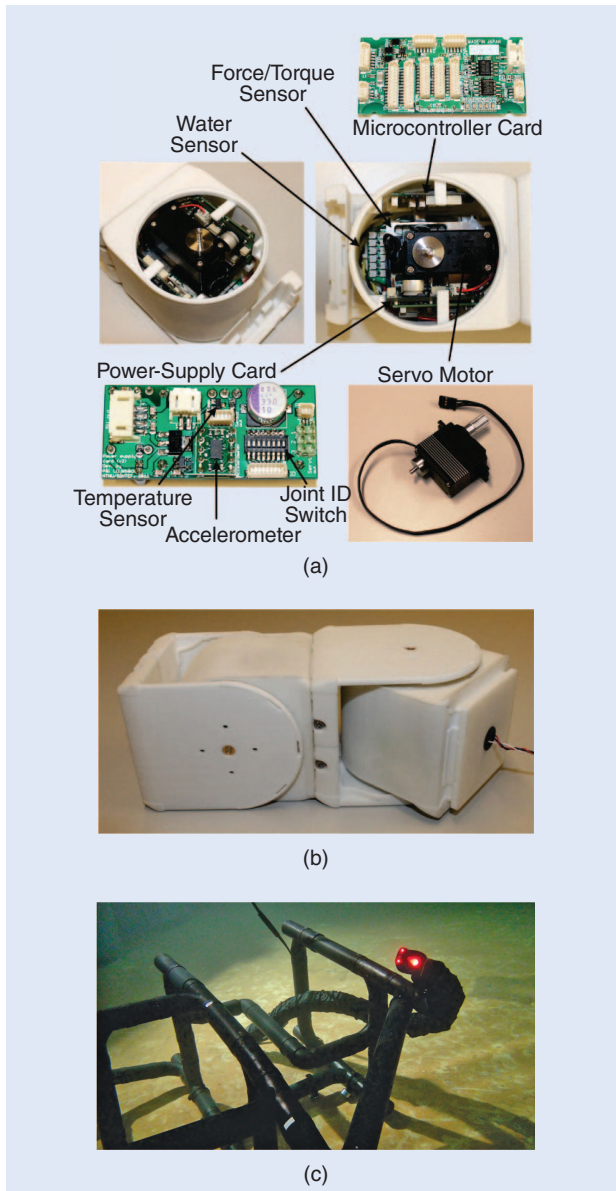


Figure 5. The underwater snake robot Mamba implemented at Norwegian University of Science and Technology to support our group's research activity about both ground and underwater snake robot locomotion: (a) the internal components of the joint module, (b) two modules connected with orthogonal joint axes, and (c) motion inside a dummy underwater structure.

Mamba (Figure 5) is a snake robot that supports our group's research activity on both ground and underwater snake robot locomotion. This flexibility results from its mechanical robustness and reconfigurable nature. The robot is watertight and has a modular design with a common mechanical and electrical interface between the modules. Each joint module is actuated by a Hitec servo motor (HSR 5990TG) and in each joint, a force/torque sensor on the joint shaft, two temperature sensors, a three-axis accelerometer and a water leakage detector, are included (Figure 5). Furthermore, each joint is controlled by means of a microcontroller card (TTTechSH2 Tiny Controller from HiBot), while the total number of microcontrollers intercommunicate over a controller area network (CAN) bus. Power-supply cables (35 V) run among the modules along with the CAN bus. A more detailed description of this robot is found in [17].

Note that all the modules of the underwater snake robot Mamba are watertight down to about 5 m. However, during the experiments, Mamba was covered by a watertight skin to achieve an extra water barrier (Figure 6). The skin is made by groundsheet, nylon, Polyurethane-coated, 120 g/m² material, and it is attached at the head and the tail using rubber bottle wrist seals, which are glued to the skin. This type of cover makes the robot's outer surface smoother, reducing drag effects. In addition, it is worth mentioning that no caudal fin is attached at the tail part of the robot during the experiments since the model presented in the "Mathematical Model of Underwater Snake Robot" section does not consider modeling of a caudal fin. Hence, the tail part only contains an anchorage mechanism for the external power-supply cable.

Setup

The experiments were performed in the Marine Cybernetics (MC)-lab in Marintek, Trondheim, Norway [53], in a tank with a length of 40 m, a height of 1.5 m, and a width of 6.45 m. To have accurate real-time measurements of the position and orientation of underwater objects, in general, the integration of a motion-capture system is essential. Thus, for our experimental process, an underwater motion-capture system from Qualisys [54] was installed in the basin, covering an underwater working area of dimensions 10 m × 1.35 m × 5.45 m.

The particular configuration of the snake robot Mamba [17] (see Figure 6) used in these experiments consisted of 18 identical joint modules mounted horizontally and vertically in an alternating fashion (Figure 5). By setting the reference angles for the joints with vertical rotating axis to be 0°, the robot was made to move according to a strictly horizontal motion pattern. In this case, the kinematics of the snake robot correspond to a planar snake robot with links of length $2l = 0.18$ m and mass $m \approx 0.8$ kg. The experiments demonstrated that the robot had a slightly positive buoyancy and was swimming near the water surface.



Figure 6. The underwater snake robot Mamba in the pool with the markers attached on the tail for position measurements.

To have accurate measurements of the robot's position and orientation, reflective markers were attached on the tail part of the robot, something that is required by the motion-capture system, as shown in Figure 6. Although the robot was swimming on the surface of the tank, the markers were submerged approximately 0.15 m under the water surface due to constraints in the covering working area imposed by the camera system. Thus, the global frame coordinates of the tail link and the absolute angle of the tail were extracted by the camera-based motion-capture system. The camera system consists of six identical cameras, which allow the reflective markers to be tracked under the water. The measured position and the absolute angle of the tail were obtained from an external computer where the Qualisys system [54] was connected, and afterward, these measurements were sent through user datagram protocol in LabVIEW 2013 to another computer, where both the fluid-parameter-identification algorithms and the path-following controller were implemented. Having the measurements of the tail position and orientation and the individual joint angles, the CM position \mathbf{p}_{CM} and the absolute link angles θ of the underwater snake robot were calculated from the kinematics equations presented in the "Mathematical Model of Underwater Snake Robot" section.

Remark 4

As previously mentioned, reflective markers were attached on the tail part of the robot to obtain the required measurements for the experiments. It is expected that the performance of the robot will be influenced by the external structure that is used to attach the reflective markers during the motion of the robot. Note that it is essential for an underwater camera system to have a stiff structure that is able to avoid any misplacement of the markers during the motion of the robot to provide accurate measurements, while the structure needs to have reasonable dimensions to reduce the effects on the motion of the robot. To reduce the influence of an external component attached to the snake, we implemented a lightweight and stiff structure made of iron ropes to

The robot is watertight and has a modular design with a common mechanical and electrical interface between the modules.

which the markers were attached. In addition, note that the camera system from Qualisys is only proper for experimental work in the lab, while, for real-life applications, available commercial solutions such as long-baseline systems, ultra-short-baseline systems, or underwater wireless sensor networks can be used. In [55], a survey of techniques for underwater localization is presented.

Model Identification

In this section, we present results regarding the fluid parameters' identification for the model of the underwater snake robot presented in the "Mathematical Model of Underwater Snake Robot" section. We obtained the values of the fluid coefficients by using the method of [14]. Note that the fluid parameters are identified to experimentally validate the closed-loop form model of underwater snake robots proposed in [2], and, in addition, it will be used for back-to-back comparison of simulation and experimental results for the path-following control strategy presented in the "LOS Path-Following Control" section.

Fluid Parameters

In [2], it is shown that the fluid force parameters, for cylindrical links with major diameter $2a$ and minor diameter $2b$ and taking into account that the length of each link is $2l$, are given by

$$c_t = \frac{1}{2} \rho \pi C_f \frac{(b+a)}{2} 2l, \quad (21)$$

$$c_n = \frac{1}{2} \rho C_D 2a 2l, \quad (22)$$

$$\mu_n = \rho \pi C_A a^2 2l, \quad (23)$$

where C_f and C_D are the drag coefficients in the x - and y -directions of motion, while C_A denotes the added mass coefficient [56] and ρ is the density of the fluid.

In addition, it is shown that the fluid torque parameters can be expressed as

$$\lambda_1 = \frac{1}{12} \rho \pi C_M (a^2 - b^2)^2 l^3, \quad (24)$$

$$\lambda_2 = \frac{1}{6} \rho \pi C_f (a + b) l^3, \quad (25)$$

$$\lambda_3 = \frac{1}{8} \rho \pi C_f (a + b) l^4, \quad (26)$$

where C_M is the added inertia coefficient.

Fluid Parameter Identification

The fluid coefficients that will be identified are C_f , C_D , and C_A . Note that the added mass inertia coefficient is set to the theoretical value $C_M = 1$ in this study since this parameter does not significantly affect the overall motion of the system [2], [25].

Using the underwater snake robot Mamba (Figure 6) with the reflective markers attached on the tail of the robot, we were able to measure the position and the orientation of the tail module by using the camera system described in

the "Experimental Setup" section. Combining these measurements with the measurements of the joint angles and using the kinematic equations presented in the "Mathematical Model of Underwater Snake Robot" section, we are able to calculate the position of the CM of the robot. As mentioned earlier, the robot is commanded to move according to a horizontal motion pattern in a horizontal plane, by setting the reference angles corresponding to the vertical joint motion to zero. Hence, only the joints with horizontal rotating axis are made to rotate, and the number of links is $n = 9$. This is because we need only measurements in the 2-D horizontal plane for the fluid coefficients identification of the 2-D fluid model presented in the "Mathematical Model of Underwater Snake Robot" section. We applied the sinusoidal motion pattern given by (17) with different parameters. In particular, in each trial, the reference joint angles were computed by (17) for $n = 9$, choosing $g(i,n) = 1$ and $g(i,n) = (n-i)/(n+1)$ in the case of lateral undulation and eel-like motion, respectively. These references were sent to the robot via the CAN. In each trial, we measured the position of the CM and the steady-state values of the achieved velocity for approximately 30 s of motion. Note that an existing proportional controller, implemented in the microcontroller of each joint module, is responsible for the control of the corresponding joint angle. Finally, the initial values of the link angles were set to zero in each experiment task, while the initial position of the robot is presented in each trial.

To perform a back-to-back comparison of experimental data and ideal simulation results, we simulated the model of the underwater snake robot presented in the "Mathematical Model of Underwater Snake Robot" section with the fluid coefficients found by curve fitting between one set of simulated data with one set of data from the motion of the physical robot, to be $C_f = 0.3$, $C_D = 1.75$, $C_A = 1.5$ for lateral undulation and $C_f = 0.17$, $C_D = 1.75$, $C_A = 1.5$ for eel-like motion. Note that the fluid coefficient C_f is smaller for the eel-like motion compared with the lateral undulation. This was expected since we have oscillations with smaller amplitude at the head of the robot, causing the effect of the drag forces in the x -direction to be smaller. In particular, we considered an underwater snake robot with $n = 9$ links, each one having length $2l = 0.18$ m and mass $m = 0.8$ kg, i.e., identical to the physical robot presented in the "Underwater Snake Robot—Mamba" section. The hydrodynamic-related parameters for the elliptic section with major and minor diameters $2a = 2 \cdot 0.055$ m and $2b = 2 \cdot 0.05$ m, respectively, and $\rho = 1,000$ kg/m³ were calculated by (21)–(26). In these simulations a joint PD-controller (20) was used with parameters $k_p = 20$, $k_d = 5$, while lateral undulation or eel-like motion were achieved by moving the joints according to (17) by choosing $g(i,n) = 1$ and $g(i,n) = (n-i)/(n+1)$, respectively, with gait parameters values similar to the ones of the experimental trials.

In Figures 7 and 8, we present simulation and experimental results that were obtained by choosing the fluid

coefficients as mentioned earlier and $\alpha = 30^\circ$, $\omega = 120^\circ/s$, $\delta = 30^\circ$, and $\phi_0 = 0$ for lateral undulation and eel-like motion. The simulated and the experimental results are expressed in the global frame with the origin being at $(0, 0)$ for visualization purposes. This makes the comparison of the simulated and the experimental results clearer, without changing the response of the system. From Figures 7(a) and 8(a), we see that the robot managed to transverse the same distance in the x -direction both in simulations and in experiments. The oscillations in the y -direction (Figures 7(b) and 8(b)) are larger in the experimental trial compared to the simulated results. This is mostly due to the inaccuracies of the sensor measurements in the experimental setup. The achieved forward steady-state velocity was calculated for the simulated and the physical robot by using

$$V_f^s = \sqrt{\dot{p}_x(t_{\text{end}})^2 + \dot{p}_y(t_{\text{end}})^2} \quad (27)$$

and

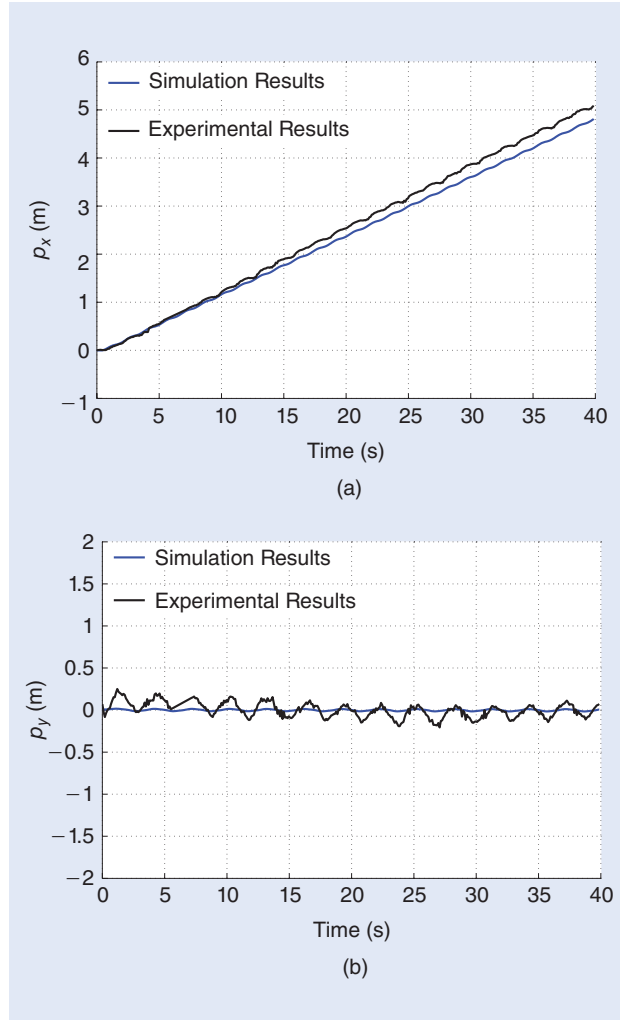


Figure 7. Lateral undulation: the comparison results of the simulated and real robot for the gait parameters $\alpha = 30^\circ$, $\omega = 120^\circ/s$, $\delta = 30^\circ$, and $\phi_0 = 0$. (a) The position along the path p_x . (b) The position along the path p_y .

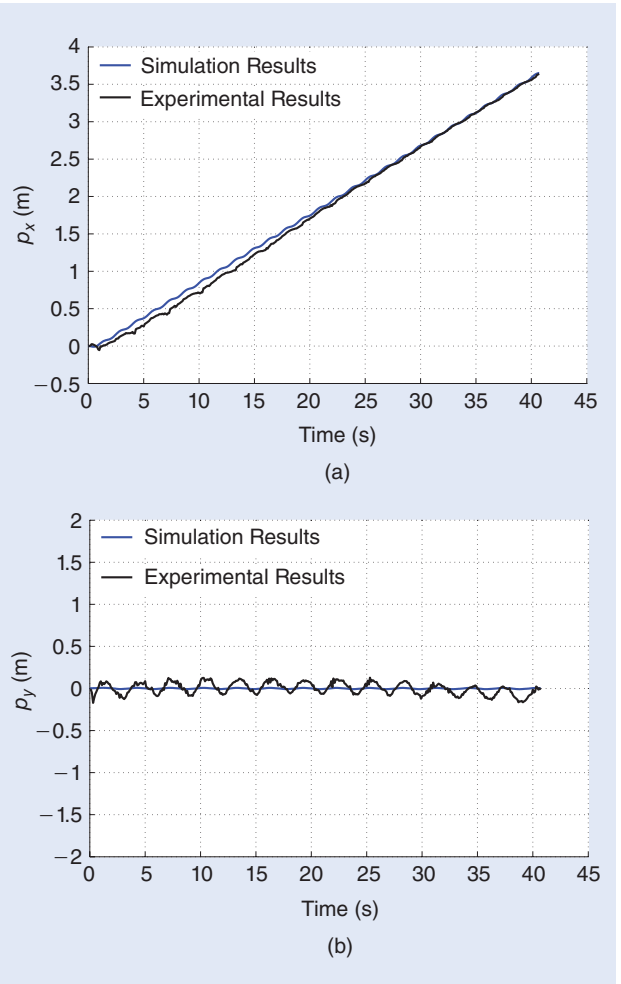


Figure 8. Eel-like motion: the comparison results of the simulated and real robot for the gait parameters $\alpha = 30^\circ$, $\omega = 120^\circ/s$, $\delta = 30^\circ$ and $\phi_0 = 0$. (a) The position along the path p_x . (b) The position along the path p_y .

Table 2. The fluid parameter identification for lateral undulation.

α	ω	δ	V_f^s	V_f^r	Error %
30	120	20	0.1207	0.1275	5.37
30	120	30	0.1275	0.1288	1.01
30	120	50	0.0851	0.0937	9.11
30	110	30	0.1153	0.1281	10.03
30	130	30	0.1252	0.1179	6.21

Table 3. The fluid parameter identification for eel-like motion.

α	ω	δ	V_f^s	V_f^r	Error %
30	120	20	0.0742	0.0756	1.88
30	120	30	0.0897	0.0894	0.33
30	120	50	0.0723	0.0738	1.98
30	110	30	0.0867	0.0996	12.92
30	130	30	0.0927	0.0885	4.81

$$V_f^r = \frac{\sqrt{(p_x(t_{\text{end}}) - p_x(t_0))^2 + (p_y(t_{\text{end}}) - p_y(t_0))^2}}{t_{\text{end}} - t_0}, \quad (28)$$

respectively. Note that t_{end} and t_0 indicate the beginning and the end of the time horizon, respectively. The amplitudes of the achieved forward steady-state velocities for the lateral undulation calculated by (27) and (28) were 0.1275 m/s and 0.1288 m/s for the simulated robot and the real robot, respectively. The error between these velocities was 1.01%, which indicates that there is quite good agreement between the simulated dynamics of the robot and the real experiments. In addition, the steady-state velocities for the eel-like motion were 0.0897 and 0.0894 m/s for the simulated robot and the real robot, respectively. The error between the velocities for the case of eel-like motion was 0.33%.

In addition, by keeping the chosen values for the fluid coefficients constant, we obtained comparable results between the simulation and experimental results both for the lateral undulation and eel-like motion pattern. In Tables 2 and 3, we can see the achieved forward velocities both for the simulated and the physical system for different values of the gait parameters. In particular, the first three columns of the tables present the values of the gait parameters, while the last three columns present the forward velocity of the simulated robot, the velocity of the physical robot and the relative error between the forward velocities, respectively. From Tables 2 and 3, we can see that the maximum error between the simulated and the physical robot was 10.03% and 12.92% for the lateral

undulation and eel-like motion pattern, respectively. These preliminary results show that the fluid coefficients are quite sensitive to variations of the gait parameters. However, in [14], it was also shown that, for the swimming speed, the discrepancies between modeling and reality do not exceed 16%.

Remark 5

Note that another, more accurate method for the fluid coefficients identification should be investigated in the future for more precise identified values of the drag and added mass coefficients since, as we can see from Tables 2 and 3, the identified fluid coefficients are quite sensitive to variations of the gait parameters. In this study, preliminary results are obtained for the model presented in the “Mathematical Model of Underwater Snake Robot” section, which mainly will be used to investigate the efficacy of the path-following controller presented in the “LOS Path-Following Control” section by comparing the experimental results with the simulated ones. In the future, the force/torque sensor installed inside the modules of the snake robot may be used to obtain more general results for the fluid coefficients, avoiding the calculation of these coefficients by fitting the simulated motion with the motion of the physical robot.

Experimental Investigation of LOS Path-Following Controller

In this section, the experimental results will be presented to investigate the efficacy of the LOS path-following controller

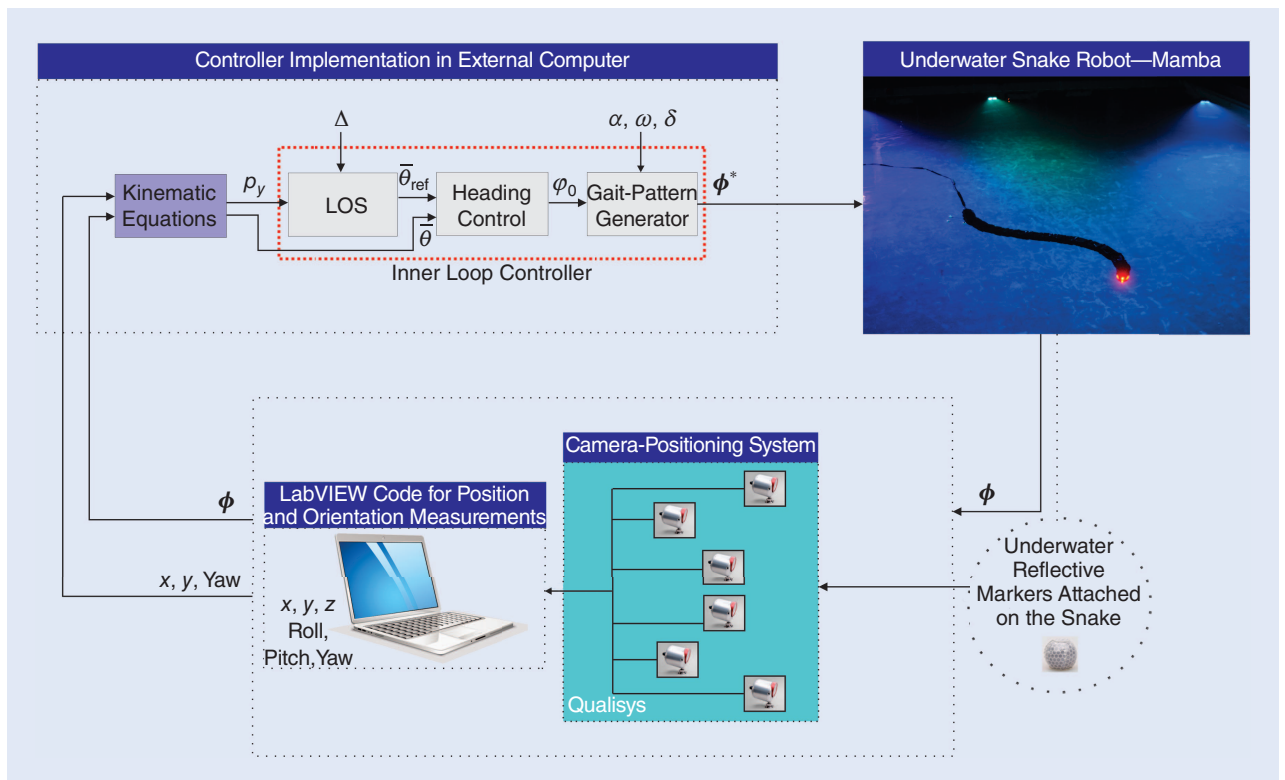


Figure 9. An illustration of the controller structure used in the experiments, with the markers attached to the tail of the robot for position measurements.

presented in the “LOS Path-Following Control” section. In particular, the performance of the guidance strategy was investigated experimentally for straight-line paths for both lateral undulation and eel-like motion patterns.

Setup for Path-Following Controller Experiments

The path-following controller was experimentally investigated using the underwater snake robot Mamba (see Figure 5).

The total control structure that was adopted in the experimental task is illustrated in Figure 9. The individual computations and the implementation of the path-following controller are described in the sequel steps. Having the measurements of the tail position and orientation, and the individual joint angles, we calculated, using the kinematics equations presented in the “Mathematical Model of Underwater Snake Robot” section, the CM position, \mathbf{p}_{CM} , and the

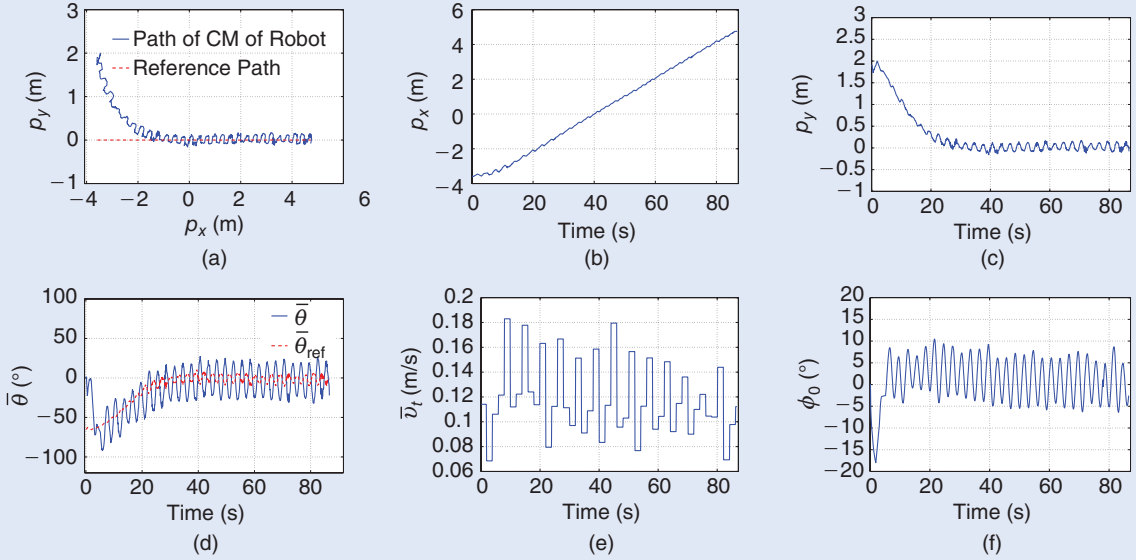


Figure 10. A straight-line path following with the physical snake initially headed along the desired path, and with the initial distance from the CM being $p_y = 1.89$ m for lateral undulation with gait parameters $\alpha = 35^\circ$, $\omega = 120^\circ/\text{s}$, and $\delta = 40^\circ$. (a) the path of the CM, (b) the position along the path p_x , (c) the cross-track error p_y , (d) the heading angle $\bar{\theta}$, (e) the forward velocity \bar{v}_t , and (f) the joint angle offset ϕ_0 .

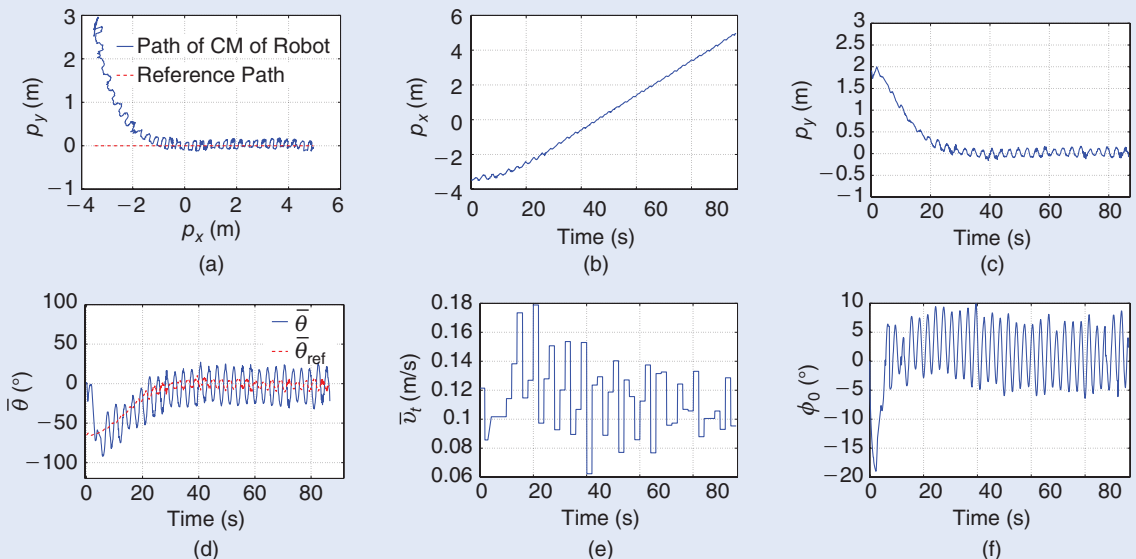


Figure 11. A straight-line path following with the physical snake initially headed along the desired path, and with the initial distance from the CM being $p_y = 2.81$ m for lateral undulation with gait parameters $\alpha = 35^\circ$, $\omega = 120^\circ/\text{s}$, and $\delta = 40^\circ$: (a) the path of the CM, (b) the position along the path p_x , (c) the cross-track error p_y , (d) the heading angle $\bar{\theta}$, (e) the forward velocity \bar{v}_t , and (f) the joint angle offset ϕ_0 .

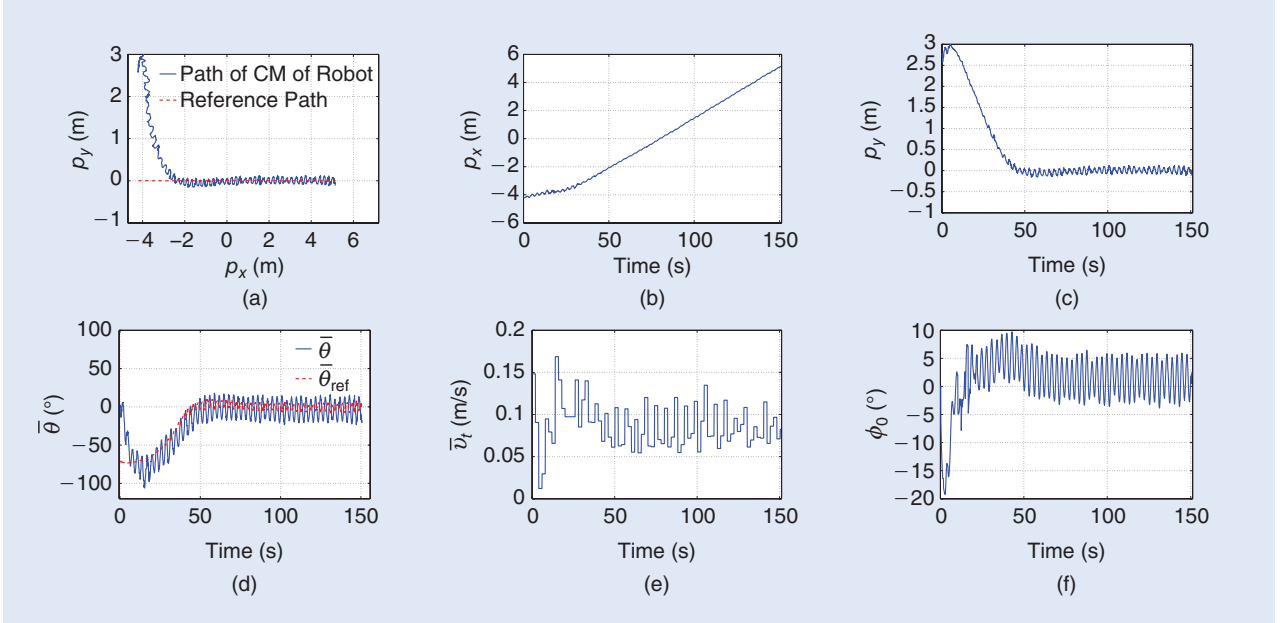


Figure 12. A straight-line path following with the physical snake initially headed along the desired path, and with the initial distance from the CM being $p_y = 2.75$ m for eel-like motion with gait parameters $\alpha = 40^\circ$, $\omega = 120^\circ/\text{s}$, and $\delta = 40^\circ$: (a) the path of the CM, (b) the position along the path p_x , (c) the cross-track error p_y , (d) the heading angle $\bar{\theta}$, (e) the forward Velocity \bar{v}_t , and (f) the joint angle offset ϕ_0 .

absolute link angles, θ , of the underwater snake robot. The LOS path-following controller of the underwater snake robot was implemented on an external computer according to (17)–(19), i.e., for the lateral undulation and eel-like motion gait patterns. Specifically, the reference joint angles, computed by (17), were sent to each joint module of the robot via the CAN bus running through the robot. A proportional controller implemented in the microcontroller of each joint module controlled the joint angle according to the received reference angle. The joint torque controller given by (20) was not implemented, since the servo motors installed in the snake robot do not require torque control input as the servos have built in angle regulation. The robot's orientation was calculated according to (2), i.e., as the average of the individual link angles.

The LOS guidance law angle given by (18) was calculated with a look-ahead distance equal to half the length of the robot, i.e., $\Delta = 0.9$ m [1] for fast convergence, due to the limited working area covered by the camera system. Furthermore, the control gain in (19) was $k_\theta = 0.4$ and $k_\phi = 0.6$ for lateral undulation and eel-like motion, respectively. The joint angle offset was saturated according to $\phi_0 = [-20^\circ, 20^\circ]$ to keep the joint reference angles within reasonable bounds and taking into account the physical robot's joint angle constraints. Moreover, the reference angles were calculated by (17) for $n = 9$ choosing $g(i, n) = 1$ and $g(i, n) = (n - i)/(n + 1)$ in the case of lateral undulation or eel-like motion, respectively, while the rest of the gait parameters were $\alpha = 35^\circ$ for lateral undulation and $\alpha = 40^\circ$ for eel-like motion, $\alpha = 40^\circ$ and $\omega = 120^\circ/\text{s}$. The initial joint angles were zero in all the trials, while the initial heading and position of the robot will be specified for each trial.

Experimental Results

The straight-line-path-following controller was experimentally investigated for both lateral undulation and eel-like motion patterns. In particular, experimental results for two different sets of initial conditions are presented here, both for lateral undulation and eel-like motion patterns. In the first four trials of the experiments, the robot was initially headed along the desired path (the x -axis), and the initial distance from the CM to the desired path was 1.89 m and 2.81 m for lateral undulation (Figures 10–11) and 2.75 m and 2.98 m for eel-like motion (Figures 12–13). In the last two trials, the robot was initially headed toward the desired path (the x -axis) with initial heading $\bar{\theta}(0) = -91.3^\circ$ and $\bar{\theta}(0) = -88.3^\circ$ for lateral undulation (Figure 14) and eel-like motion (Figure 15), and the initial distance from the CM to the desired path was 1.59 m and 1.97 m, respectively. The xy -plots of the experimental results for the different trials are presented in Figures 10(a), 11(a), and 14(a) for lateral undulation and Figures 12(a), 13(a), and 15(a) for eel-like motion pattern, where it is easily seen that the robot converged nicely toward and moved along the desired path during all trials both for lateral undulation and eel-like motion patterns. In particular, we can see that the CM of the underwater snake robot converged to the desired path for all the trials.

In Figures 10(d)–15(d), we can see that (19) made the heading angle converge to and oscillate around zero for both lateral undulation and eel-like motion patterns. Moreover, Figures 10(c)–15(c) show that the cross-track error converged to and oscillated around zero. Furthermore, the forward velocity of the robot is shown in Figures 10(e)–15(e) and the joint angle offset is shown in Figures 10(f)–15(f).

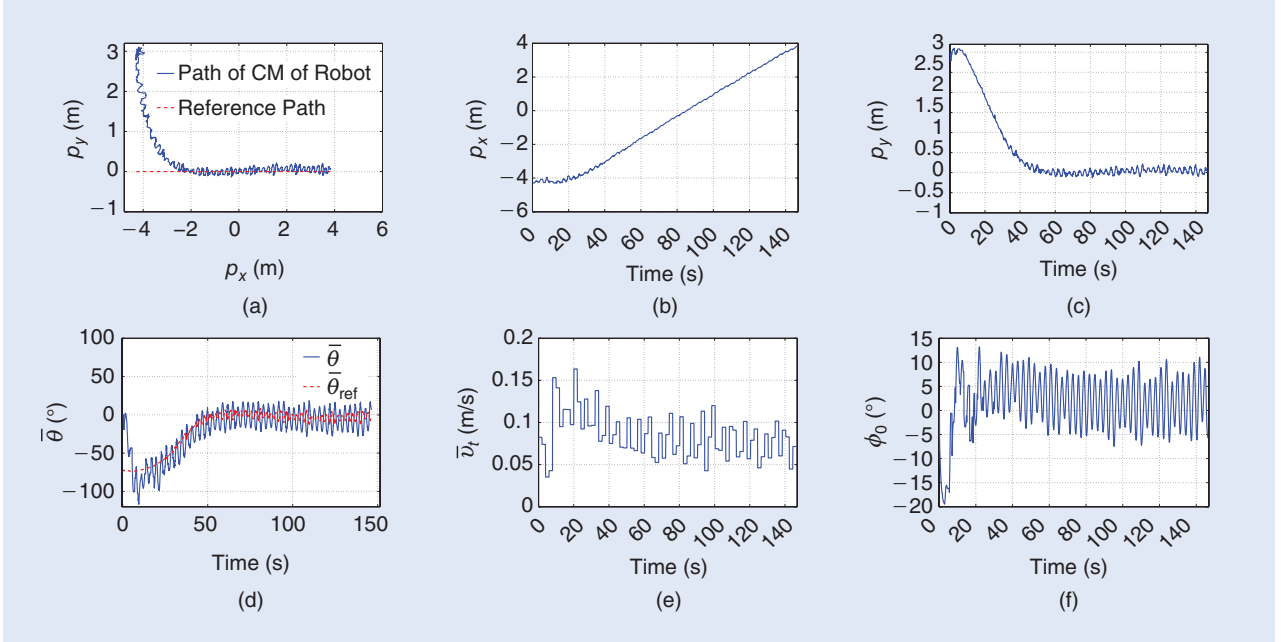


Figure 13. A straight-line path following with the physical snake initially headed along the desired path, and with the initial distance from the CM being $p_y = 2.98$ m for eel-like motion with gait parameters $\alpha = 40^\circ$, $\omega = 120^\circ/\text{s}$, and $\delta = 40^\circ$: (a) the path of the CM, (b) the position along the path p_x , (c) the cross-track error p_y , (d) the heading angle $\bar{\theta}$, (e) the forward velocity \bar{v}_t , and (f) the joint angle offset ϕ_0 .

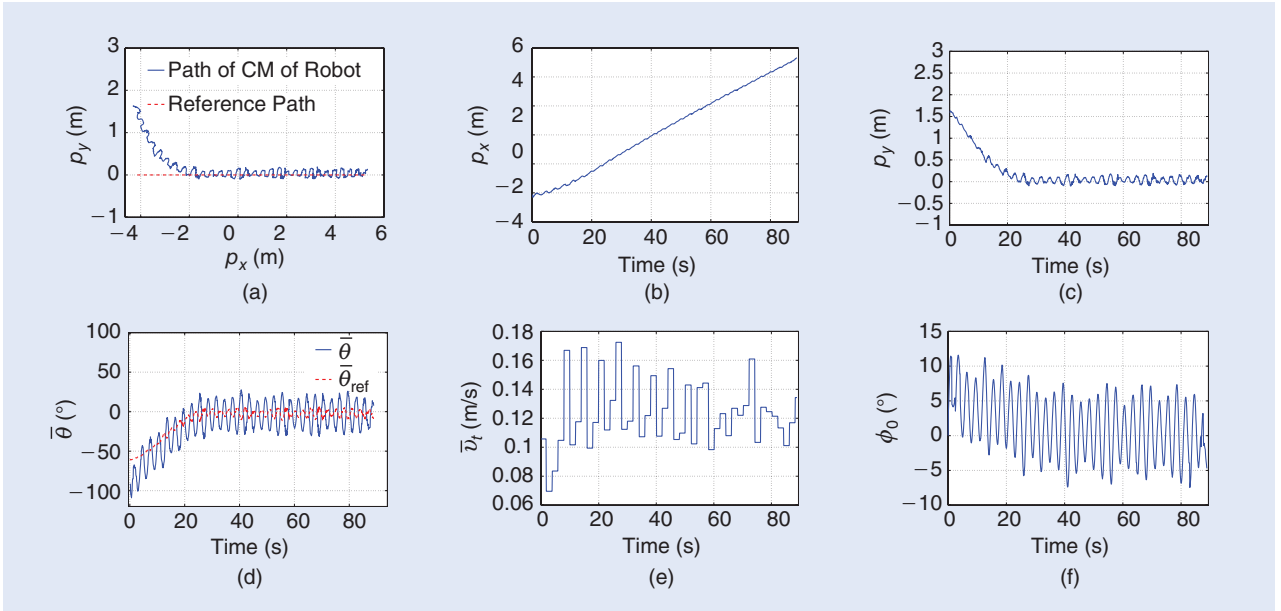


Figure 14. A straight-line path following with the physical snake initially headed toward the desired path, and with the initial heading and the distance from the CM $\bar{\theta}(0) = -91.3^\circ$, $p_y = 1.59$ m, respectively, for lateral undulation with gait parameters $\alpha = 35^\circ$, $\omega = 120^\circ/\text{s}$ and $\delta = 40^\circ$: (a) the path of the CM, (b) the position along the path p_x , (c) the cross-track error p_y , (d) the heading angle $\bar{\theta}$, (e) the forward velocity \bar{v}_t , and (f) the joint angle offset ϕ_0 .

Figures 10–15 clearly show that the heading, the cross-track error, and the position of the robot achieved a steady-state oscillatory behavior when the robot reached the desired path. Note that this was as expected since, for snake robots, forward locomotion is achieved using a sinusoidal gait pattern, and it is then not possible to achieve a purely nonoscillatory motion of the CM [57]. Similar to the oscillatory

behavior of the CM, the orientation of the robot was also expected to oscillate, as shown in Figures 10(d)–15(d).

The visualizations in Figures 16 and 17 for the results presented in Figures 10 and 12 for lateral undulation and eel-like motion, respectively, illustrate that the robot converged nicely toward and moved along the desired path. This claim is supported by the plots of the cross-track error in Figures 10(c)

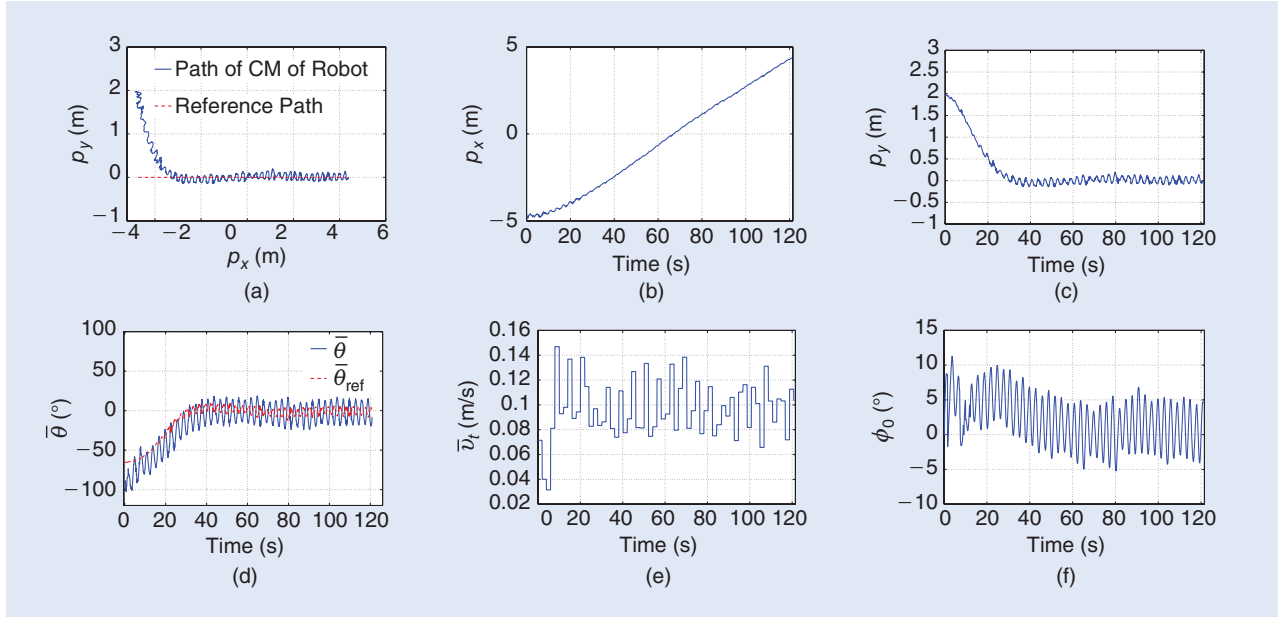


Figure 15. A straight-line path following with the physical snake initially headed toward the desired path, and with the initial heading and the distance from the CM being $\theta(0) = -88.3^\circ$ and $p_y = 1.97$ m respectively, for eel-like motion with gait parameters $\alpha = 40^\circ$, $\omega = 120^\circ/\text{s}$ and $\delta = 40^\circ$: (a) the path of the CM, (b) the position along the path p_x , (c) the cross-track error p_y , (d) the heading angle $\bar{\theta}$, (e) the forward velocity \bar{v}_t , and (f) the joint angle offset ϕ_0 .

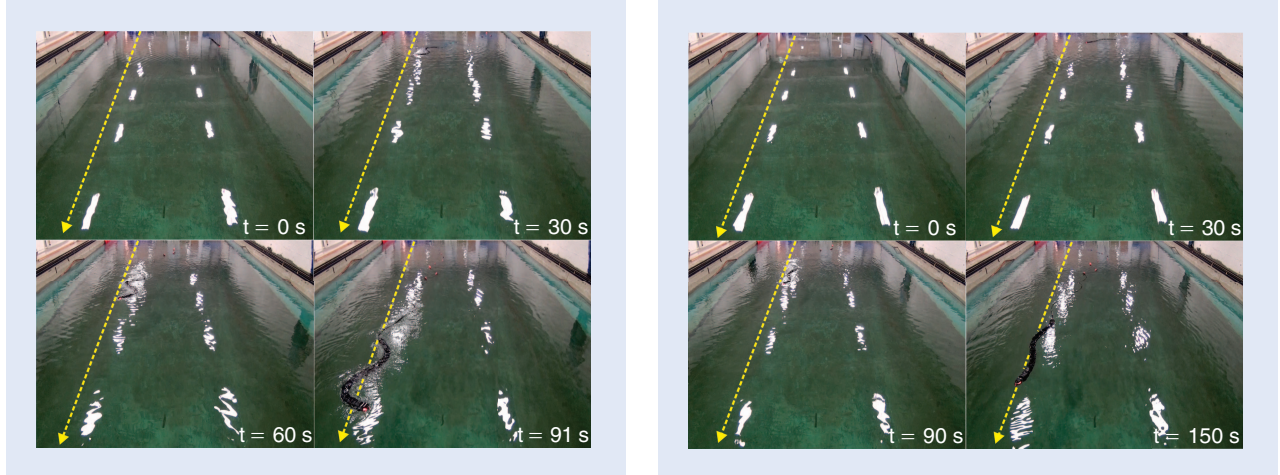


Figure 16. The motion of the underwater snake robot during path following for the experimental results presented in Figure 10. The yellow line indicates the desired path, i.e., the global x -axis.

and 12(c), which shows that the cross-track error converged to and oscillated about zero.

Simulation Results

To perform a back-to-back comparison of real experimental and ideal simulation results, we simulated the model presented in the “Mathematical Model of Underwater Snake Robot” section with the LOS path-following controller proposed in the “LOS Path-Following Control” section using similar parameters as in the experiments. In particular, we considered an underwater snake robot with $n = 9$ links, each one having length $2l = 0.18$ m and mass $m = 0.8$ kg, i.e., identical to the physical robot presented in the “Experimental Setup”

Figure 17. The motion of the underwater snake robot during path following for the experimental results presented in Figure 12. The yellow line indicates the desired path, i.e., the global x -axis.

section. The hydrodynamic parameters $c_t, c_n, \mu_n, \lambda_1, \lambda_2$ and λ_3 were calculated for the fluid coefficients C_f, C_d , and C_A as identified in the “Model Identification” section. The joint PD controller (20) was used for each joint with parameters $k_p = 20, k_d = 5$, and the reference angles corresponding to the horizontal joint motion of the robot were calculated according to (17) with $n = 9$ by choosing $g(i, n) = 1$ and $g(i, n) = (n - i)/(n + 1)$ for lateral undulation and eel-like motion respectively, with the same gait parameters as presented in the “Fluid Parameter Identification” section. Furthermore, the control gain in (19) is $k_\theta = 0.4$ and $k_\theta = 0.6$ for lateral undulation and eel-like motion, respectively, while the guidance law parameter in (18)

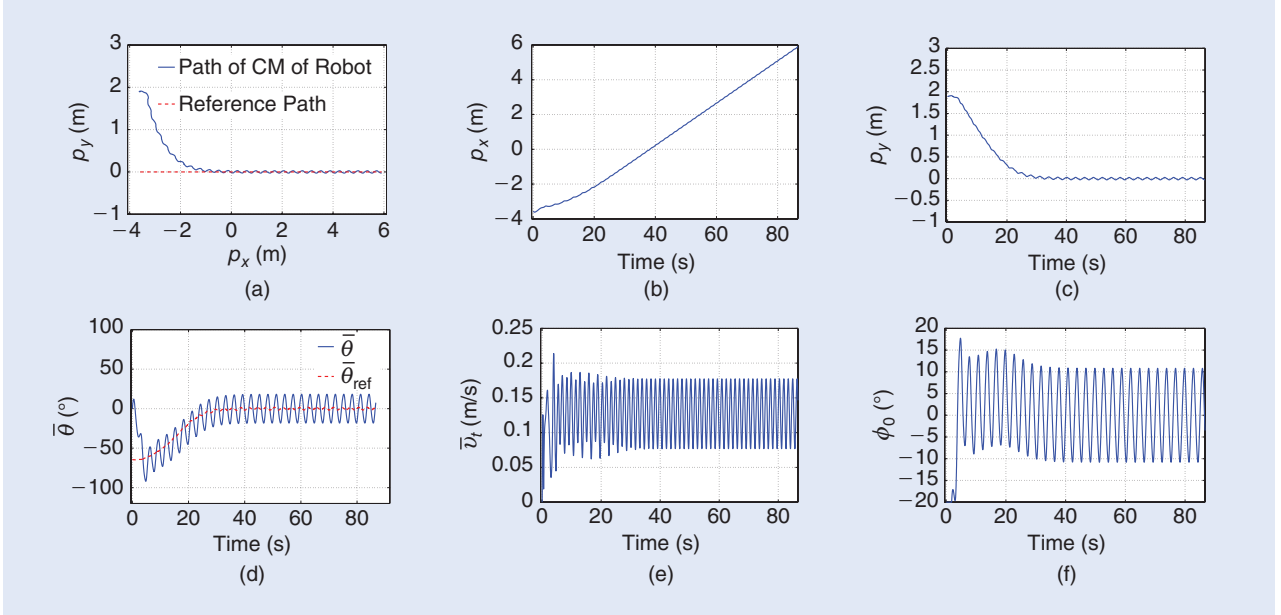


Figure 18. The simulation results for straight-line path following for a snake robot with $n = 9$ links initially headed along the desired path, and with the initial distance from the CM being $p_y = 1.89$ m for lateral undulation with gait parameters $\alpha = 35^\circ$, $\omega = 120^\circ/\text{s}$ and $\delta = 40^\circ$: (a) the path of the CM, (b) the position along the path p_x , (c) the cross-track error p_y , (d) the heading angle $\bar{\theta}$, (e) the forward velocity \bar{v}_t , and (f) the joint angle offset ϕ_0 .

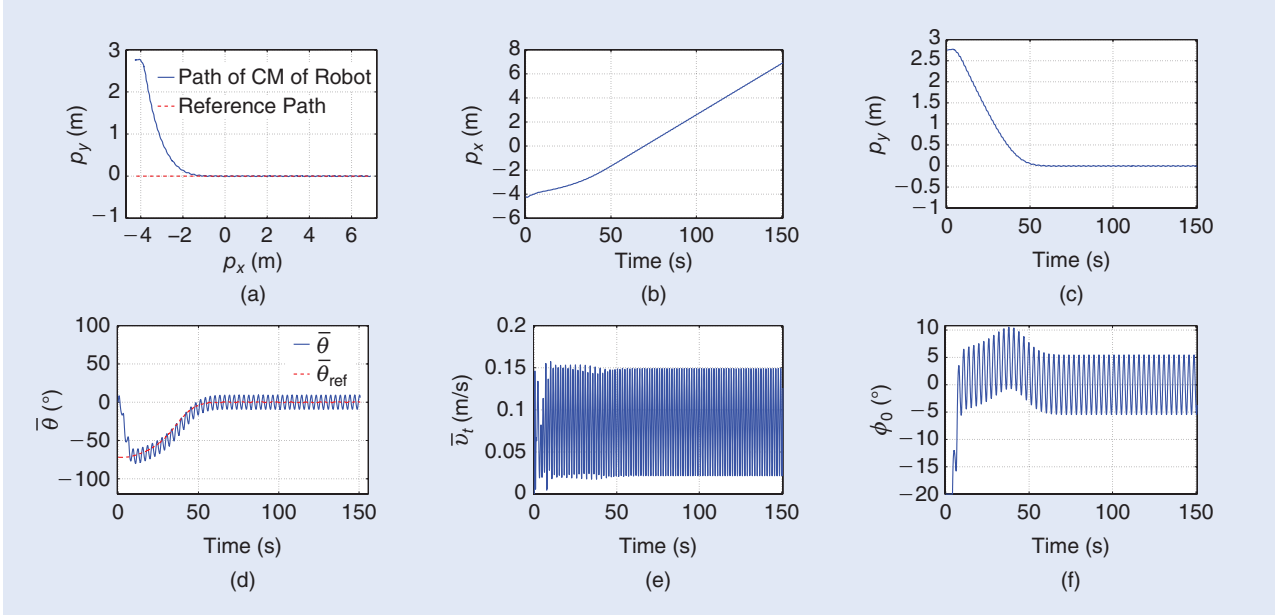


Figure 19. The simulation results for straight-line path following for a snake robot with $n = 9$ links initially headed along the desired path, and with the initial distance from the CM being $p_y = 2.75$ m for eel-like motion with gait parameters $\alpha = 40^\circ$, $\omega = 120^\circ/\text{s}$ and $\delta = 40^\circ$: (a) the path of the CM, (b) the position along the path p_y , (c) the cross-track error p_y , (d) the heading angle $\bar{\theta}$, (e) the forward velocity \bar{v}_t , and (f) the joint angle offset ϕ_0 .

was chosen as $\Delta = 0.9$ similar to the experimental trials. The initial values of all states of the robot were set to zero except for the initial position of the CM, which was selected as $\mathbf{p}_{\text{CM}}(0) = [-3.58, 1.89]$ and $\mathbf{p}_{\text{CM}}(0) = [-4.20, 2.75]$ for lateral undulation and eel-like motion, respectively, i.e., the same as the initial values of the experiments presented in Figures 10 and 12. The simulation results are shown in Figures 18 and 19. In addition, Figures 20 and 21 present the

comparison results for the cross-track error and the heading between the simulated and the physical robot.

The results shown in Figures 18–21 indicate that the qualitative behavior of the simulated system is similar to the behavior of the physical robot. In particular, from Figures 10(a), 12(a) and Figures 18(a), 19(a) it can be seen that the physical snake and the simulated snake followed almost the same path for both lateral undulation and eel-like motion

patterns. The cross-track error converged and oscillated around zero for both motion patterns, as shown in Figures 10(c), 12(c), and 20(b) and Figures 18(c), 19(c), and 21(b). The cross-track error in Figures 10(c) and 12(c) has larger oscillations compared to the ideal case in Figures 18(c) and

**An eel-like motion can be
achieved by propagating
lateral axial undulations
with increasing amplitude
from head to tail.**

21(a), we see that, in both cases, the heading converged zero. The oscillations of the heading are larger in Figures 10(d) and 12(d) than in Figures 18(d) and 19(d), and this is again due to the inaccuracies of the different measurements from the sensors. Note that the heading is defined as the average of the link angles (2), and any inaccurate measurements from the encoders will produce errors; this is the main reason for the larger oscillations in the heading in the experimental results presented in Figures 10(d) and 12(d).

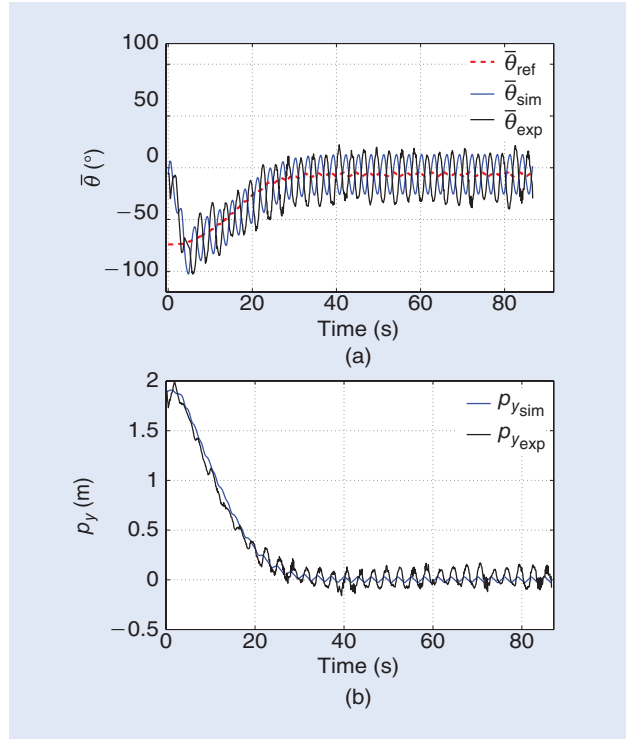


Figure 20. The comparison results for straight-line path following for a snake robot with $n = 9$ links initially headed along the desired path, and with the initial distance from the CM being $p_y = 2.75$ m for lateral undulation with gait parameters $\alpha = 35^\circ$, $\omega = 120^\circ/\text{s}$ and $\delta = 40^\circ$: (a) the cross-track error p_y and (b) the heading angle $\bar{\theta}$.

Remark 6

It should be noted that, in [34] and [41], to investigate the performance of the path-following control strategies, the fluid coefficients were chosen under the assumption of a steady-state flow [36], [58]. In this article, however, simulation results for the LOS path-following controller are performed for the drag and added mass coefficients of the system identified experimentally in the “Model Identification” section.

Remark 7

Comparing the experimental results (Figures 10 and 12) with the simulated ones (Figures 18 and 19), we see that the simulated model reached higher velocities both for lateral undulation and eel-like motion. This was mainly due to the power-supply cable that was attached to the robot. Note that, in our simulations, we did not have the extra drag effects that were produced from the power-supply cable of the physical robot that was used in the experiments. The effect of this cable is more visible for the slower motion achieved for the eel-like motion pattern (Figures 12 and 19). However, the comparison results presented in Figures 20 and 21 show good agreement between the simulated and the physical robot for the cross-track error and the heading both for lateral undulation and eel-like motion patterns.

Conclusions and Future Work

In this article, experimental results for LOS path-following control of biologically inspired swimming snake robots

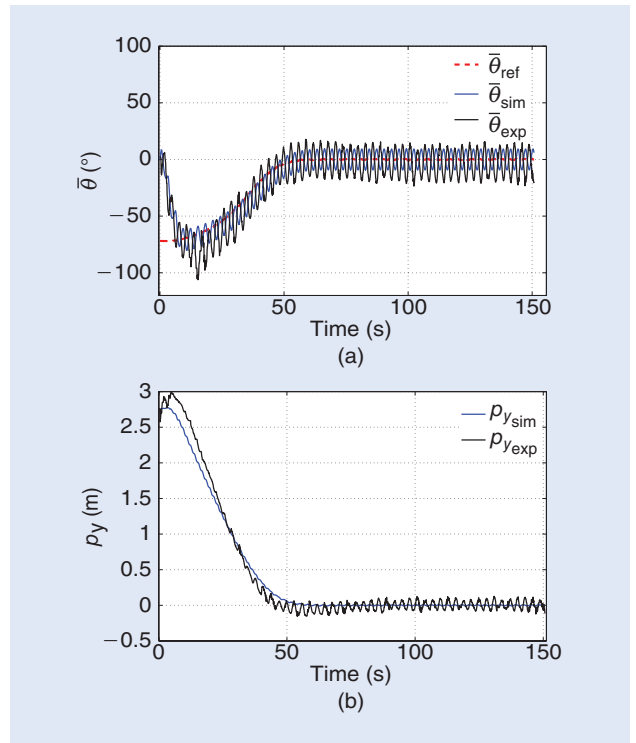


Figure 21. The comparison results for straight-line path following for a snake robot with $n = 9$ links initially headed along the desired path, and with the initial distance from the CM being $p_y = 2.75$ m for eel-like motion with gait parameters $\alpha = 40^\circ$, $\omega = 120^\circ/\text{s}$ and $\delta = 40^\circ$: (a) the cross-track error p_y and (b) the heading angle $\bar{\theta}$.

were presented. In particular, a straight-line-path-following controller was proposed for an underwater snake robot, both for lateral undulation and eel-like motion patterns. The LOS guidance law was combined with a directional controller to steer the robot to the path. The proposed path following controller consists of three main components: 1) the gait-pattern controller, which produces a sinusoidal motion pattern that propels the robot forward, 2) the heading controller, which steers the robot toward and subsequently along the desired path, and 3) the LOS guidance law, which generates the desired heading angle to follow the desired path. It was shown that the proposed control scheme could be applied to underwater snake robots to achieve path following of straight lines. In addition, fluid parameter identification was performed and simulation results based on the identified fluid coefficients were presented to obtain a back-to-back comparison with the motion of the physical robot during the experiments. The experimental results showed that the proposed control strategy successfully steers the robot toward and along the desired path for both lateral undulation and eel-like motion patterns.

In future work, the authors will investigate the validity of the proposed control strategy for general path-following control purposes. In this article, we did not take into account the current effects since there is no possibility to produce current at the MC-lab. It is furthermore of interest to test the scheme for the fluid coefficient identification in combination with current effects in the future. The force/torque sensors installed inside the modules of the robot may be used for more precise online fluid coefficient identification with and without the current effects. In addition, an interesting topic for future work concerns the possibility to extend the proposed control approach to 3-D and thus be able to investigate depth control strategies for underwater snake robots. An experimental investigation of path following of underwater snake robots in 3-D is necessary to realize underwater snake robots for challenging real-time subsea operations.

Acknowledgments

This work was partly supported by the Research Council of Norway through project 205622 and its Centres of Excellence funding scheme project 223254-NTNU AMOS.

References

- [1] T. I. Fossen, *Handbook of Marine Craft Hydrodynamics and Motion Control*. Hoboken, NJ: Wiley, 2011.
- [2] E. Kelasidi, K. Y. Pettersen, J. T. Gravdahl, and P. Liljebäck, "Modeling of underwater snake robots," in *Proc. IEEE Int. Conf. Robotics Automation*, Hong Kong, China, May 31–June 7, 2014, pp. 4540–4547.
- [3] P. Liljebäck, K. Y. Pettersen, Ø. Stavdahl, and J. T. Gravdahl, *Snake Robots: Modelling, Mechatronics, and Control*. Berlin, Germany: Springer-Verlag, Advances in Industrial Control, 2013.
- [4] P. Liljebäck, K. Y. Pettersen, Ø. Stavdahl, and J. T. Gravdahl, "A review on modelling, implementation, and control of snake robots," *Robot. Autonomous Syst.*, vol. 60, no. 1, pp. 29–40, 2012.
- [5] A. A. Transeth and K. Y. Pettersen, "Developments in snake robot modeling and locomotion," in *Proc. 9th Int. Conf. Control, Automation, Robotics and Vision*, Singapore, Dec. 5–8, 2006, pp. 1–8.
- [6] J. Gray, "Studies in animal locomotion," *J. Exp. Biol.*, vol. 10, no. 1, pp. 88–104, 1933.
- [7] S. Hirose, *Biologically Inspired Robots: Snake-Like Locomotors and Manipulators*. London, U.K.: Oxford Univ. Press, 1993.
- [8] S. Hirose and H. Yamada, "Snake-like robots [tutorial]," *IEEE Robot. Automat. Mag.*, vol. 16, no. 1, pp. 88–98, 2009.
- [9] R. Crespi, A. Badertscher, A. Guignard, and A. J. Ijspeert, "Amphibot I: an amphibious snake-like robot," *Robot. Autonomous Syst.*, vol. 50, no. 4, pp. 163–175, 2005.
- [10] P. Liljebäck, K. Y. Pettersen, and Ø. Stavdahl, "A snake robot with a contact force measurement system for obstacle-aided locomotion," in *Proc. IEEE Int. Conf. Robotics Automation*, Anchorage, AK, May 3–7, 2010, pp. 683–690.
- [11] K. Melsaac and J. Ostrowski, "A geometric approach to anguilliform locomotion: modelling of an underwater eel robot," in *Proc. Int. Conf. Robotics Automation*, Detroit, MI, May 10–15, 1999, vol. 4, pp. 2843–2848.
- [12] K. McIsaac and J. Ostrowski, "Experiments in closed-loop control for an underwater eel-like robot," in *Proc. IEEE Int. Conf. Robotics Automation*, Washington, DC, May 12–18, 2002, pp. 750–755.
- [13] A. Crespi and A. J. Ijspeert, "AmphiBot II: An amphibious snake robot that crawls and swims using a central pattern generator," in *Proc. 9th Int. Conf. Climbing Walking Robots*, Brussels, Belgium, Sept. 2006, pp. 19–27.
- [14] M. Porez, F. Boyer, and A. J. Ijspeert, "Improved lighthill fish swimming model for bio-inspired robots: Modeling, computational aspects and experimental comparisons," *Int. J. Robot. Res.*, vol. 33, no. 10, pp. 1322–1341, 2014.
- [15] C. Ye, S. Ma, B. Li, and Y. Wang, "Locomotion control of a novel snake-like robot," in *Proc. IEEE/RSJ Int. Conf. Intelligent Robots Systems*, Sendai, Japan, Sept. 28–Oct. 2, 2004, vol. 1, pp. 925–930.
- [16] H. Yamada, S. Chigasaki, M. Mori, K. Takita, K. Ogami, and S. Hirose, "Development of amphibious snake-like robot ACM-R5," in *Proc. 36th Int. Symp. Robotics*, TH3C4, 2005.
- [17] P. Liljebäck, Ø. Stavdahl, K. Pettersen, and J. Gravdahl, "Mamba—A waterproof snake robot with tactile sensing," in *Proc. Int. Conf. Intelligent Robots Systems*, Chicago, IL, Sept. 14–18, 2014, pp. 294–301.
- [18] K. Morgansen, B. Triplett, and D. Klein, "Geometric methods for modeling and control of free-swimming fin-actuated underwater vehicles," *IEEE Trans. Robot.*, vol. 23, no. 6, pp. 1184–1199, 2007.
- [19] M. Kruusmaa, P. Fiorini, W. Megill, M. De Vittorio, O. Akanyeti, F. Visentin, L. Chambers, H. El Daou, M.-C. Fiazza, J. Jezov, M. Listak, L. Rossi, T. Salumae, G. Toming, R. Venturelli, D. Jung, J. Brown, F. Rizzi, A. Qualtieri, J. Maud, and A. Liszewski, "Filose for svanning: A flow sensing bioinspired robot," *IEEE Robot. Automat. Mag.*, vol. 21, no. 3, pp. 51–62, 2014.
- [20] G. Taylor, "Analysis of the swimming of long and narrow animals," *Proc. Royal Soc. London. Ser. A. Math. Phys. Sci.*, vol. 214, no. 1117, pp. 158–183, 1952.
- [21] M. J. Lighthill, "Large-amplitude elongated-body theory of fish locomotion," *Proc. Royal Soc. London. Ser. B. Biol. Sci.*, vol. 179, no. 1055, pp. 125–138, 1971.
- [22] K. McIsaac and J. Ostrowski, "Motion planning for anguilliform locomotion," *IEEE Trans. Robot. Automat.*, vol. 19, no. 4, pp. 637–625, 2003.
- [23] F. Boyer, M. Porez, and W. Khalil, "Macro-continuous computed torque algorithm for a three-dimensional eel-like robot," *IEEE Trans. Robot.*, vol. 22, no. 4, pp. 763–775, 2006.
- [24] J. Chen, W. O. Friesen, and T. Iwasaki, "Mechanisms underlying rhythmic locomotion: Body-fluid interaction in undulatory swimming," *J. Exp. Biol.*, vol. 214, no. 4, pp. 561–574, 2011.

- [25] A. Wiens and M. Nahon, "Optimally efficient swimming in hyperredundant mechanisms: Control, design, and energy recovery," *Bioinspir. Biomim.*, vol. 7, no. 4, p. 046016, 2012.
- [26] J. Blair and T. Iwasaki, "Optimal gaits for mechanical rectifier systems," *IEEE Trans. Autom. Contr.*, vol. 56, no. 1, pp. 59–71, 2011.
- [27] F. Candelier, M. Porez, and F. Boyer, "Note on the swimming of an elongated body in a non-uniform flow," *J. Fluid Mech.*, vol. 716, pp. 616–637, Feb. 2013.
- [28] L. Zhu, Z. Chen, and T. Iwasaki, "Oscillation, orientation, and locomotion of underactuated multilink mechanical systems," *IEEE Trans. Contr. Syst. Technol.*, vol. 21, no. 5, pp. 1537–1548, 2013.
- [29] J. Colgate and K. Lynch, "Mechanics and control of swimming: A review," *IEEE J. Oceanic Eng.*, vol. 29, no. 3, pp. 660–673, 2004.
- [30] J. Liu and H. Hu, "Biological inspiration: from carangiform fish to multi-joint robotic fish," *J. Bionic Eng.*, vol. 7, pp. 35–48, 2010.
- [31] R. Clapham and H. Huosheng, "iSplash-II: Realizing fast carangiform swimming to outperform a real fish," in *Proc. IEEE/RSJ Int. Conf. Intelligent Robots Systems*, Chicago, IL, Sept. 14–18, 2014, pp. 1080–1086.
- [32] D. Jung, P. Pott, T. Salumae, and M. Kruusmaa, "Flow-aided path following of an underwater robot," in *Proc. IEEE Int. Conf. Robotics Automation*, Karlsruhe, Germany, May 6–10, 2013, pp. 4602–4607.
- [33] Y. Ding, S. S. Sharpe, A. Masse, and D. I. Goldman, "Mechanics of undulatory swimming in a frictional fluid," *PLoS Comput. Biol.*, vol. 8, no. 12, p. e1002810, 2012.
- [34] E. Kelasidi, P. Liljebäck, K. Y. Pettersen, and J. T. Gravdahl, "Integral line-of-sight guidance for path following control of underwater snake robots: Theory and experiments," *IEEE Trans. Robot.*, 2014, Submitted for publication.
- [35] O. Ekeberg, "A combined neuronal and mechanical model of fish swimming," *Biol. Cybern.*, vol. 69, no. 5–6, pp. 363–374, 1993.
- [36] W. Khalil, G. Gallot, and F. Boyer, "Dynamic modeling and simulation of a 3-D serial eel-like robot," *IEEE Trans. Syst., Man, Cybern., Part C: Applcat. Rev.*, vol. 37, no. 6, pp. 1259–1268, 2007.
- [37] E. Kelasidi, K. Y. Pettersen, P. Liljebäck, and J. T. Gravdahl, "Integral line-of-sight for path-following of underwater snake robots," in *Proc. IEEE Multi-Conf. Systems Control*, Juan Les Antibes, France, Oct. 8–10, 2014, pp. 1078–1085.
- [38] K. McIsaac and J. Ostrowski, "Open-loop verification of motion planning for an underwater eel-like robot," in *Experimental Robotics VII*, (series Lecture Notes in Control and Information Sciences, no. 271), D. Rus and S. Singh, Eds. Berlin, Germany: Springer-Verlag, 2001, pp. 271–280.
- [39] P. A. Vela, K. A. Morgansen, and J. W. Burdick, "Underwater locomotion from oscillatory shape deformations," in *Proc. 41st IEEE Conf. Decision Control*, vol. 2, Las Vegas, USA, Dec. 10–13, 2002, pp. 2074–2080.
- [40] K. McIsaac and J. Ostrowski, "A framework for steering dynamic robotic locomotion systems," *Int. J. Robot. Res.*, vol. 22, no. 2, pp. 83–97, 2003.
- [41] E. Kelasidi, K. Y. Pettersen, and J. T. Gravdahl, "A waypoint guidance strategy for underwater snake robots," in *Proc. IEEE 22nd Mediterranean Conf. Control Automation*, Palermo, Italy, June 16–19, 2014, pp. 1512–1519.
- [42] J. Guo, "A waypoint-tracking controller for a biomimetic autonomous underwater vehicle," *Ocean Eng.*, vol. 33, no. 17–18, pp. 2369–2380, 2006.
- [43] M. Alamir, M. El Rafei, G. Hafidi, N. Marchand, M. Porez, and F. Boyer, "Feedback design for 3D movement of an eel-like robot," in *Proc. IEEE Int. Conf. Robotics Automation*, Roma, Apr. 10–14, 2007, pp. 256–261.
- [44] M. El Rafei, M. Alamir, N. Marchand, M. Porez, and F. Boyer, "Motion control of a three-dimensional eel-like robot without pectoral fins," in *Proc. 17th IFAC World Congr.*, 2008, vol. 17, no. 1, pp. 750–755.
- [45] M. El Rafei, M. Alamir, N. Marchand, M. Porez, and F. Boyer, "Multi-variable constrained control approach for a threedimensional eel-like robot," in *Proc. IEEE/RSJ Int. Conf. Intelligent Robots Systems*, Nice, France, Sept. 22–26, 2008, pp. 3152–3157.
- [46] L. Lapierre and B. Jouvel, "Path following control for an eel-like robot," in *Proc. MTS/IEEE Int. Conf. Oceans*, Brest, France, June 20–23, 2005, vol. 1, pp. 460–465.
- [47] E. Kelasidi, K. Y. Pettersen, and J. T. Gravdahl, "Energy efficiency of underwater snake robot locomotion," in *Proc. 23rd Mediterranean Conf. Control Automation*, Torremolinos, Spain, June 16–19, 2015.
- [48] E. Kelasidi, K. Y. Pettersen, and J. T. Gravdahl, "Energy efficiency of underwater robots," in *Proc. 10th IFAC Conf. Manoeuvring Control Marine Craft*, Copenhagen, Denmark, Aug. 24–26, 2015, pp. 1124–1131.
- [49] E. Kelasidi, K. Y. Pettersen, and J. T. Gravdahl, "Stability analysis of underwater snake robot locomotion based on averaging theory," in *Proc. IEEE Int. Conf. Robotics Biomimetics*, Bali, Indonesia, Dec. 5–10, 2014, pp. 574–581.
- [50] E. Kelasidi and A. Tzes, "Serpentine motion control of snake robots for curvature and heading based trajectory - parameterization," in *Proc. IEEE 20th Mediterranean Conf. Control Automation*, Barcelona, Spain, July 3–6, 2012, pp. 536–541.
- [51] E. Borhaug, A. Pavlov, and K. Pettersen, "Integral LOS control for path following of underactuated marine surface vessels in the presence of constant ocean currents," in *Proc. 47th IEEE Conf. Decision Control*, Cancun, Dec. 9–11, 2008, pp. 4984–4991.
- [52] E. Fredriksen and K. Y. Pettersen, "Global k-exponential way-point maneuvering of ships: Theory and experiments," *Automatica*, vol. 42, no. 4, pp. 677–687, 2006.
- [53] [2016, Feb. 4]. Marine cybernetics laboratory (MC-lab). [Online]. Available: <http://www.ntnu.no/imt/lab/cybernetics>
- [54] [2016, Feb. 4]. Qualisys—motion capture systems. [Online]. Available: <http://www.qualisys.com>
- [55] H.-P. Tan, R. Diamant, W. K. Seah, and M. Waldmeyer, "A survey of techniques and challenges in underwater localization," *Ocean Eng.*, vol. 38, no. 1415, pp. 1663–1676, 2011.
- [56] J. Newman, *Marine Hydrodynamics*. Cambridge, MA: MIT Press, 1977.
- [57] P. Liljeback, K. Pettersen, O. Stavdahl, and J. Gravdahl, "Controllability and stability analysis of planar snake robot locomotion," *IEEE Trans. Autom. Contr.*, vol. 56, no. 6, pp. 1365–1380, 2011.
- [58] C. Jordan, "Coupling internal and external mechanics to predict swimming behavior: A general approach," *Amer. Zoologist*, vol. 36, no. 6, pp. 710–722, 1996.

Eleni Kelasidi, Centre for Autonomous Marine Operations and Systems, Norwegian University of Science and Technology, Trondheim, Norway. E-mail: eleni.kelasidi@itk.ntnu.no.

Pål Liljeback, Centre for Autonomous Marine Operations and Systems, Norwegian University of Science and Technology, Norway. E-mail: pal.liljeback@itk.ntnu.no.

Kristin Y. Pettersen, Centre for Autonomous Marine Operations and Systems, Norwegian University of Science and Technology, Norway. E-mail: Kristin.Y.Pettersen@itk.ntnu.no.

Jan Tommy Gravdahl, Norwegian University of Science and Technology, Trondheim, Norway. E-mail: tommy.gravdahl@itk.ntnu.no.